visicoil.com

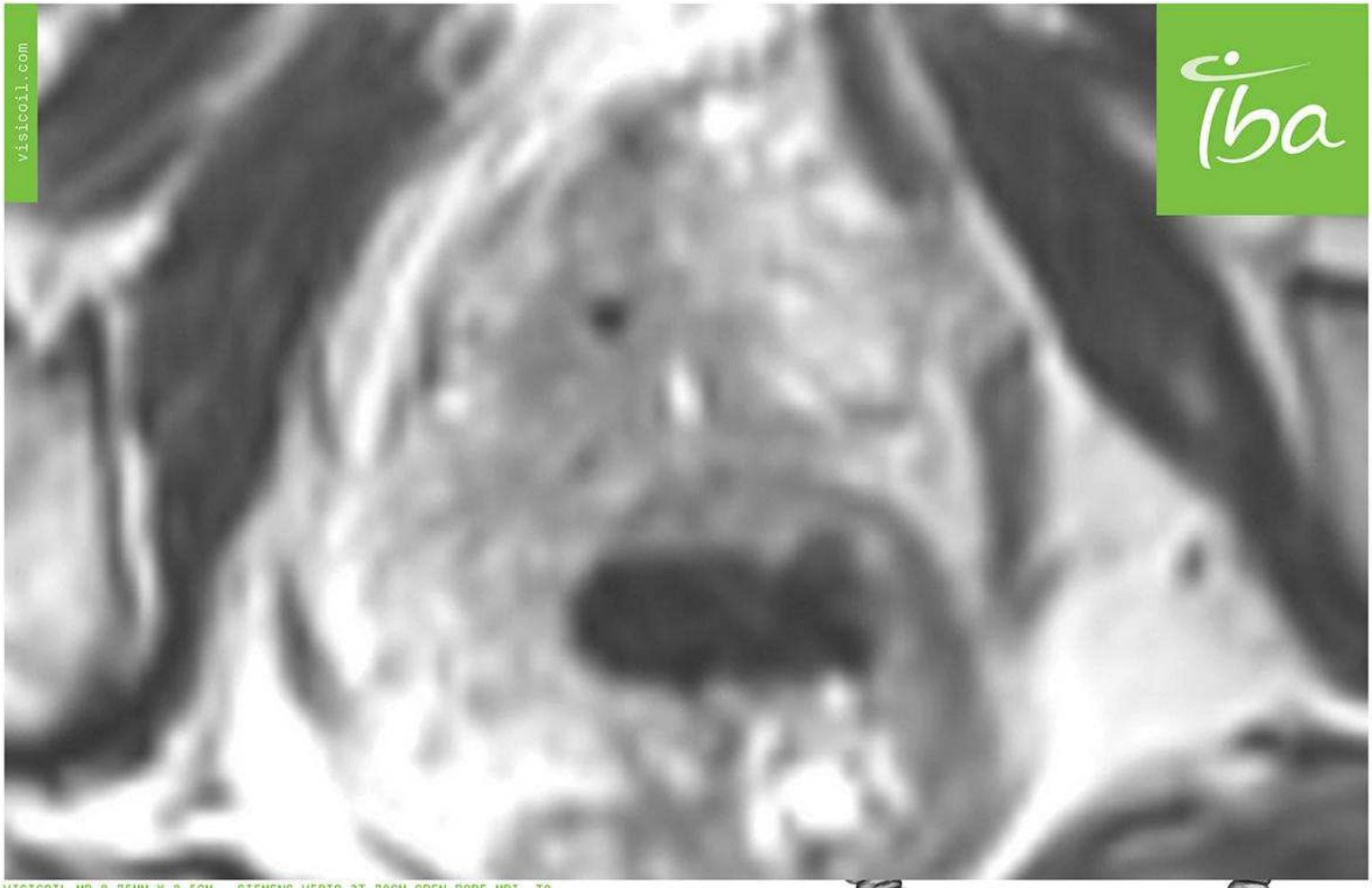

VISICOIL MR 0.75MM X 0.5CM SIEMENS VERIO 3T 70CM OPEN BORE MRI, T2

VISICOIL™ MR

"new"

Multi-modality linear fiducial marker
Enhanced for greater MRI visibility

SEE IT!
Enhanced MR Visibility = Easier MR/CT fusion

TRUST IT!
Reliable = Accurate localization from implant -> treatment

TREAT IT!
Smaller Needles = Safer implants & improved patient comfort

VISIT IBA BOOTH 5083 AT AAPM 2017 TO LEARN MORE

PROTECT +
ENHANCE +
SAVE LIVES

Anatomical noise in contrast-enhanced digital mammography. Part I. Single-energy imaging

Melissa L. Hill[a)]
Sunnybrook Research Institute, 2075 Bayview Avenue, Toronto, Ontario M4N 3M5, Canada and Department of Medical Biophysics, University of Toronto, 2075 Bayview Avenue, Toronto, Ontario M4N 3M5, Canada

James G. Mainprize
Sunnybrook Research Institute, 2075 Bayview Avenue, Toronto, Ontario M4N 3M5, Canada

Ann-Katherine Carton and Serge Muller
GE Healthcare, 283 rue de la Minière, Buc 78530, France

Mehran Ebrahimi
Faculty of Science, University of Ontario Institute of Technology, 2000 Simcoe Street North, Oshawa, Ontario L1H 7K4, Canada

Roberta A. Jong
Breast Imaging, Sunnybrook Health Sciences Centre, 2075 Bayview Avenue, Toronto, Ontario M4N 3M5, Canada

Clarisse Dromain
Department of Radiology, Institut Gustave Roussy, 39 rue Camille Desmoulin, Villejuif 94805, France

Martin J. Yaffe
Sunnybrook Research Institute, 2075 Bayview Avenue, Toronto, Ontario M4N 3M5, Canada and Department of Medical Biophysics, University of Toronto, 2075 Bayview Avenue, Toronto, Ontario M4N 3M5, Canada

(Received 6 November 2012; revised 21 March 2013; accepted for publication 29 March 2013; published 23 April 2013)

Purpose: The use of an intravenously injected iodinated contrast agent could help increase the sensitivity of digital mammography by adding information on tumor angiogenesis. Two approaches have been made for clinical implementation of contrast-enhanced digital mammography (CEDM), namely, single-energy (SE) and dual-energy (DE) imaging. In each technique, pairs of mammograms are acquired, which are then subtracted with the intent to cancel the appearance of healthy breast tissue to permit sensitive detection and specific characterization of lesions. Patterns of contrast agent uptake in the healthy parenchyma, and uncanceled signal from background tissue create a "clutter" that can mask or mimic an enhancing lesion. This type of "anatomical noise" is often the limiting factor in lesion detection tasks, and thus, noise quantification may be useful for cascaded systems analysis of CEDM and for phantom development. In this work, the authors characterize the anatomical noise in CEDM clinical images and the authors evaluate the influence of the x-ray energy used for acquisition, the presence of iodine in the breast, and the timing of imaging postcontrast administration on anatomical noise. The results are presented in a two-part report, with SE CEDM described here, and DE CEDM in Part II.

Methods: A power law is used to model anatomical noise in CEDM images. The exponent, β, which describes the anatomical structure, and the constant α, which represents the magnitude of the noise, are determined from Wiener spectra (WS) measurements on images. A total of 42 SE CEDM cases from two previous clinical pilot studies are assessed. The parameters α and β are measured both from unprocessed images and from subtracted images.

Results: Consistent results were found between the two SE CEDM pilot studies, where a significant decrease in β from a value of approximately 3.1 in the unprocessed images to between about 1.1 and 1.8 in the subtracted images was observed. Increasing the x-ray energy from that used in conventional DM to those of typical SE CEDM spectra with mean energies above 33 keV significantly decreased α by about a factor of 19, in agreement with theory. Compared to precontrast images, in the unprocessed postcontrast images at 30 s postinjection, α was larger by about 7.4×10^{-7} mm^2 and β was decreased by 0.2. While α did not vary significantly with the time after contrast administration, β from the unprocessed image WS increased linearly, and β from subtracted image WS increased with an initial quadratic relationship that plateaued by about 5 min postinjection.

Conclusions: The presence of an iodinated contrast agent in the breast produced small, but significant changes in the power law parameters of unprocessed CEDM images compared to the precontrast images. Image subtraction in SE CEDM significantly reduced anatomical noise compared to

conventional DM, with a reduction in both α and β by about a factor of 2. The data presented here, and in Part II of this work, will be useful for modeling of CEDM backgrounds, for systems characterization and for lesion detectability experiments using models that account for anatomical noise.
 [http://dx.doi.org/10.1118/1.4801905]

Key words: beta, anatomical noise, power-law, contrast-enhanced, mammography

I. INTRODUCTION

In mammography, the projection of x rays through ducts, lobules, blood vessels, and stroma interposed by adipose tissue in the breast, creates complex patterns in the image, which can obscure the visualization of tumors. The texture of such patterns has been characterized by several investigators as following a power-law dependence on spatial frequency.[1–7] They have proposed that the structure in a mammogram follows the relationship:

$$\mathrm{WS}(f) \propto \frac{\alpha}{(cf)^{\beta}}, \tag{1}$$

where $\mathrm{WS}(f)$ is the Wiener Spectrum (WS) of a mammogram over spatial frequencies, f, α is a constant proportional to the magnitude of the noise, c is a constant scale factor that is assumed to be 1 with units inverse to f, making the denominator dimensionless, and β is the power law exponent, with a value related to the structure of breast tissues in the mammogram. The c term will be taken to be implicit for the remainder of this work such that α will have units equivalent to the WS. Burgess and others have shown that the detectability of mass-lesions in mammographic backgrounds is inversely proportional to the magnitude of β.[2,8–10] Similarly, a decreased value of α in medical images has been shown to significantly improve lesion detectability.[11,12] Therefore, it is anticipated that methods to reduce the anatomical noise in mammography should increase detection performance.

One approach to reducing the anatomical noise in a mammogram, while at the same time obtaining functional information and increasing lesion conspicuity, is contrast-enhanced digital mammography (CEDM). In CEDM exams, a nonionic, iodinated contrast agent is administered intravenously and image pairs are acquired for subtraction. The image acquisition and subsequent image subtraction can be performed according to two different methods. In the first, one precontrast image is acquired and then after intravenous injection of the contrast agent, one or more postcontrast images are acquired. We will refer to this as single-energy (SE) CEDM imaging because all of the images in an exam are acquired with the same x-ray spectrum. This spectrum has a high-energy (HE) compared to that normally used for mammography, with a mean energy above the k-edge of iodine at 33.2 keV to maximize the image contrast between the breast tissue and iodinated contrast agents. Pre and postcontrast image pairs are logarithmically subtracted and the resultant images provide at least partial cancelation of the appearance of normal tissue, and the residual signal represents regions of contrast agent uptake.[13] An alternative method is dual-energy (DE) imaging, where the contrast agent is administered and then two images are acquired in rapid succession, a HE image and a low-energy (LE) image, with the mean x-ray energies of the two spectra above and below the k-edge of iodine, respectively. An appropriately weighted combination of these two images produces a DE image with signal proportional to the iodine thickness and, similar to SE CEDM, largely cancels the appearance of the normal parenchyma.[14]

CEDM succeeds in increasing lesion conspicuity, and reducing the anatomical structure in the subtraction mammogram due to differences between contrast agent uptake in normal parenchyma and tumor tissue. In the development of malignant lesions, the formation of a vascular supply is required for growth beyond about 1 mm^3 in size to provide essential oxygen and nutrients.[15] This new vasculature tends to be poorly formed, with gaps in the endothelium about 100 nm in size, which is about 100 times larger than the pore size of cellular junctions in normal endothelium.[16,17] These large openings in the endothelium allow contrast agents to preferentially leak out of tumor vasculature into the extravascular-extracellular space (EES) of cancers, leading to increased x-ray attenuation at the site of cancers, and a resultant bright lesion signal in CEDM images compared to the surrounding tissue. This property may be useful to help differentiate cancerous and benign lesions of the basis of their contrast agent uptake patterns; either by spatially varying patterns such as rim-enhancement, or by temporally varying patterns such as rapid uptake and washout as compared to a slow and steady enhancement.[18–20]

A number of factors can lead to incomplete cancelation of the normal tissue structure in CEDM, including differences in the proportion of x-ray scatter in HE and LE images for DE imaging,[21] the polyenergetic nature of the x-ray beam,[13] patient motion between image acquisitions,[22] and the overall presence of contrast agent in the tissue (background).[18] The effect of x-ray scatter in DE CEDM can largely be eliminated by correction for scatter in the images before combination,[23] and because in DE imaging the two images are acquired in rapid succession there is less potential for breast motion compared to SE CEDM. However, all implementations of CEDM that use the standard, small-molecule contrast agents are subject to the limitation of the presence of contrast agent in the normal tissues.[24,25] Breast magnetic resonance imaging (MRI), which also uses freely diffusible contrast agents, similarly suffers from this limitation, and it has been noted in the literature on this modality that the amount of background enhancement varies with a woman's hormonal status and breast density,[24,25] and increased parenchymal enhancement is associated with a higher abnormal interpretation rate.[26,27]

In this work, we aim to quantify the anatomical noise in normal breast tissue in CEDM images in terms of the power

law parameters, α and β. An estimate of anatomical noise is an important component in cascaded systems analysis,[11,12] and knowledge of the anatomical noise in CEDM is important for the development of both physical and software phantoms for use in quality control and system evaluation.[28–31] Recently, some investigators have included an estimate of CEDM anatomical noise in models for system optimization with the assumption that the value of β is the same in CEDM as that found in mammography, but that the value of α is reduced.[32,33] While the breast tissue structure itself remains unchanged during a CEDM exam, we postulate that contrast agent uptake modifies the image WS by its nonuniform distribution across tissue types.[34–36] Here, we test the hypothesis that for the same breast, the structure of the anatomical noise, and hence, β, is different in a mammogram compared to that in a subtracted CEDM image, by measuring the power law parameters in clinical CEDM images.

We present the anatomical noise measurements in a two-part report. In this paper, Part I, we estimate the power law parameters of clinical images acquired with the SE CEDM technique. In Part II, we will describe the anatomical noise in DE images and compare the SE and DE CEDM approaches. For SE CEDM, the anatomical noise is measured in each of the precontrast, postcontrast, and log-subtracted images. We evaluate the influence on the anatomical noise of the x-ray spectrum used for image acquisition, the presence of contrast agent in the breast tissue, and the time after contrast agent administration.

II. THEORY

In CEDM polyenergetic x-ray beams are used for image acquisition. For simplicity of notation, the following theory will be derived in terms of monoenergetic approximations of the polyenergetic implementation, where energy-dependence is identified according to the mean energy of the x-ray spectrum. In a mammogram, the parenchymal pattern is related to the distribution of the breast tissue, which can be described by an x-ray attenuation equation,[37]

$$I(x, y, E) = I_0(E)\exp\{-[\mu_{\text{adipose}}(E) + \Delta\mu_{\text{B}}(E)\theta(x, y)]T\}, \quad (2)$$

where an x-ray beam of mean energy, E, that generates an open-field image signal, I_0, is attenuated by a breast with thickness, T, that is assumed to be constant over the area of interest, but the fibroglandular tissue fraction varies with a spatial distribution, $\theta(x, y) \in [0, 1]$. The differential linear x-ray attenuation coefficient, $\Delta\mu_{\text{B}}$, is the difference in linear x-ray attenuation coefficients between fibroglandular and adipose tissues. Mainprize and Yaffe demonstrated that when the spectral density of the $\theta(x, y)$ distribution follows a power law, as in Eq. (1), the resultant pattern in simulated images is a good representation of mammographic structure.[37]

In CEDM, an iodinated contrast agent is intravenously administered and is known to distribute within two main tissue compartments, the vascular space (VS) and the EES,[38] as a function of time according to patient physiology (i.e., dependent on such factors as body mass, heart rate) and the injection protocol (i.e., bolus length, use of power injector vs manual injection). The contrast agent uptake would modify the image in the following fashion:

$$I_{\text{C}}(x, y, E, t) = I(x, y, E)\exp\{-\mu_{\text{CA}}(x, y, E, t)T\}, \quad (3)$$

where $I(x, y, E)$ is the breast attenuation without contrast agent as defined in Eq. (2), and the linear x-ray attenuation coefficient due to the contrast agent concentration at time, t, at location (x, y) in the tissue is given by μ_{CA}. Because the contrast agent is assumed to be distributed throughout the breast thickness, T, the contrast agent linear attenuation, μ_{CA}, is defined here as the product of the local volumetric iodine concentration and the mass attenuation coefficient of the contrast agent.

Naïvely, one could assume equal uptake proportions for all tissue. However, it is known that the contrast agent distribution is nonuniform by tissue type. Not all of the tissue will take up agent. In fact, for any tissue type (e.g., adipose or fibroglandular), we assume that uptake only occurs in that fraction of tissue that is either EES or VS. By convention, the VS component is grouped with fibroglandular tissue, which includes the x-ray attenuation of all nonadipose normal breast tissues (excluding skin).[39] The relative fraction of EES in adipose tissue, $\lambda_{\text{EES,adipose}}$, and fibroglandular tissue, $\lambda_{\text{EES,fg}}$, will be different.[34,35,40] Furthermore, the tree-like structure of the VS (Ref. 41) differs somewhat from the spatial distribution of the other fibroglandular tissue components, where several lobes of grape-like lobule clusters are suspended within a matrix of connective stroma and adipose tissue.[42] Taking into consideration the unique structures for each tissue type, a variation on Eq. (3) can be derived that accounts for contrast agent spatial distribution

$$I_{\text{C}}(x, y, E, t) = I(x, y, E)\exp\left\{-\left[\begin{array}{c}\mu_{\text{CA,EES}}(E, t)(\lambda_{\text{EES,adipose}}[1 - \theta(x, y)] + \lambda_{\text{EES,fg}}\theta_{\text{G}}(x, y)) \\ +\mu_{\text{CA,VS}}(E, t)\theta_{\text{VS}}(x, y)\end{array}\right]T\right\}, \quad (4)$$

where the linear attenuation coefficients of the contrast agent, $\mu_{\text{CA,EES}}$ and $\mu_{\text{CA,VS}}$ in the EES and in the VS are written separately to distinguish their time-varying concentrations. The total contribution from the EES in the adipose compartment is $\lambda_{\text{EES,adipose}}[1 - \theta(x, y)]T$. The fibroglandular tissue component is further broken into the vascular component,

$\theta_{VS}(x, y)$, and that representing all other fibroglandular tissues, $\theta_G(x, y)$, such that $\theta(x, y) = \theta_{VS}(x, y) + \theta_G(x, y)$. The total contribution from the EES of the fibroglandular component is, $\lambda_{EES,fg}\theta_G(x, y)T$.

It can be shown that SE subtracted CEDM images, I_{SE}, can be generated from a pair of input images as[13]

$$I_{SE}(x, y, t) = \log[I_{C,t>0}(x, y)] - \log[I_{t0}(x, y)], \quad (5)$$

where I_{t0} and $I_{C,t>0}$ are, respectively, precontrast and postcontrast SE CEDM images acquired with a HE x-ray spectrum. We will use the convention of referring to the input mammograms as "unprocessed" images to indicate that they have not been subtracted. The postcontrast images are acquired at a time, t, after contrast agent administration, which is defined to be injected at $t = 0$ s.

To a first order approximation, the WS for SE subtracted images is given by a summation of the autocorrelation of each input image, and their cross-correlations to account for the correlated signals between the precontrast and postcontrast images:[11,43]

$$WS_{SE}(f_x, f_y) = WS_{t0}(f_x, f_y) + WS_{C,t>0}(f_x, f_y) - S(f_x, f_y)_{t0,t>0} - S(f_x, f_y)_{t>0,t0}, \quad (6)$$

where $S_{t0,\,t>0}$ and $S_{t>0,\,t0}$ are the cross-correlations of I_{t0} on $I_{C,\,t>0}$, and $I_{C,\,t>0}$ on I_{t0}, respectively, which are negative due to the subtraction in Eq. (5) (subtraction is equivalent to a filter of $-\delta$ in Ref. 43). In a generalized form, the total WS from an individual mammogram, I, can be written in terms of its constituent independent noise sources as[11]

$$WS_I(f_x, f_y) = WS_Q(f_x, f_y) + WS_{add}(f_x, f_y) + WS_{An}(f_x, f_y)MTF^2(E, f_x, f_y), \quad (7)$$

where the image WS components are, respectively, quantum noise, WS_Q, additive electronic noise, WS_{add}, and the intrinsic subject anatomical noise, WS_{An}, which is blurred by the system modulation transfer function, MTF. In this work, evaluation of the image WS is limited to a special frequency regime where the anatomical noise dominates the WS.[1] Thus, to simplify the image WS derivation, we have omitted the effects of sampling and system blur on quantum noise, and components of the electronic noise. The WS for the subtracted images, WS_{SE}, can then be further divided into their independent noise sources as[11]

$$WS_{SE}(f_x, f_y) = 2WS_Q(f_x, f_y) + 2WS_{add}(f_x, f_y) + WS^{SE}_{An}(f_x, f_y)MTF^2(E, f_x, f_y), \quad (8)$$

where spatial fluctuations of uncanceled signals in the subtracted images are captured by WS^{SE}_{An}, the residual anatomical noise components for the SE images, respectively, and the additive electronic noise and quantum components have been grouped based on the assumption that they are the same for each image.

III. MATERIALS AND METHODS

III.A. Clinical image dataset

Clinical SE CEDM images from two pilot studies were evaluated in this work.[18,19] One pilot study was led by Dr. Roberta Jong at Sunnybrook Health Sciences Centre (SHSC) in Toronto, Canada. Images from 22 women at an average age of 58 (range, 35–75) were included for anatomical noise measurement. The women were recruited for a SE CEDM exam on the basis that they were scheduled for biopsy because of suspicious masses or calcifications. The other pilot study was led by Dr. Clarisse Dromain at Institut Gustave Roussy (IGR) in Villejuif, France. The SE CEDM images from a group of 20 women with BIRADS category 4 or 5 lesions and an average age of 62 (range, 42–80) were evaluated for anatomic noise. Full details of the study designs, the image acquisition protocols, and findings for 32 of these women are described elsewhere (see cases 9–14, 16, and 18–22 within the Table of Ref. 18, and all cases in Table I of Ref. 19). For both studies, images were included in this analysis if they contained an area representing apparently normal tissue that covered at least half of the breast and that this area was sufficiently large for reliable anatomical noise evaluation (see Sec. III.B.1).

Image acquisition was carried out in both studies using a modified Senographe 2000D mammography system (GE Healthcare, Chalfont St. Giles, UK) operated with a kilovoltage of 45–49 kV, selected according to breast thickness and composition, with a Mo anode, filtered by 0.3 mm Cu and 0.3 mm Al. The same exposure per image was used in each study for breasts with equivalent characteristics, and a kilovoltage of about 46 kV was employed most often among the subjects. In the Dromain *et al.* study the total average glandular dose of the seven image procedure ranged between 1 and 4 mGy.[19] The breast was positioned in the craniocaudal (CC) view under light compression and a single precontrast image was acquired, immediately following which an injection of 100 ml of iohexol contrast agent (Omnipaque 300, GE Healthcare) was made via catheter into the antecubital vein of the arm contralateral to the breast of concern. The average compressed breast thickness for the 42 subjects was 5.8 cm. The injection procedures and the image acquisition protocols differ between the two studies in terms of timing and number of postcontrast images. A summary comparison of the imaging protocols is illustrated in Fig. 1.

In the Jong *et al.* study the contrast agent was administered manually over a period of approximately 1 min. Immediately after completion of the injection (~1 min), the first postcontrast image was obtained, and then subsequent images were obtained at 3, 5, 7, and 10 min after the initiation of contrast administration. It should be noted that in 9 of the 22 exams, one additional x-ray exposure was made prior to commencement of the CEDM study, but under the same breast compression. In these nine cases, the first image was acquired with technique factors equivalent to a conventional screening digital mammogram (DM), usually with a Rh anode and Rh filter and a tube potential of about 30 kV.

In the Dromain *et al.* study, the contrast agent was administered using a power injector (Vistron CT, Medrad), at a rate

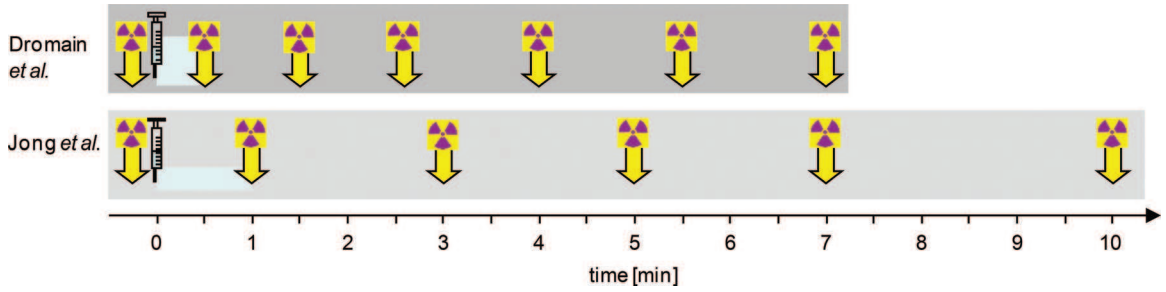

FIG. 1. Schematic of contrast agent injection and image acquisition protocols for Jong *et al*. (Ref. 18) and Dromain *et al*. (Ref. 19) SE CEDM pilot studies. The time of each image acquisition is indicated by an arrow. The start of contrast agent injection is signified by the syringe, and the duration of the injection is illustrated by a hatched bar.

of 3 ml/s, over a period of just over 30 s. The first postcontrast image was obtained 30 s after starting the injection, and subsequent mammograms were obtained at 1.5, 2.5, 4, 5.5, and 7 min. postinjection. This protocol is illustrated in a schematic in Fig. 1, alongside that of the Jong *et al*. study for a comparison of the timings of the contrast agent administrations and the image acquisitions between the two trials.

All clinical images used in this study were de-identified for use, and at the time of the clinical studies, approvals were granted by the Research Ethics Boards at SHSC and IGR, and all patients gave their written informed consent for use of the images.

III.A.1. Pre- and postcontrast image registration

An advantage of SE CEDM imaging compared to DE CEDM, is that for the same total radiation dose from an exam, a larger number of postcontrast time points may be sampled, which can reveal functional information about a lesion that may improve specificity.[18,19] However, the drawback to this approach is the potential for motion artifact in the subtracted images. Motion artifact comes from breast tissue signal that is correlated within an image pair, but that is not canceled upon image combination because of tissue movement between exposures. This artifact is seen as residual, uncanceled breast tissue in the CEDM subtracted images, with bright and dark adjacent regions where the tissue has shifted.

Patient motion during the SE CEDM exams was sometimes significant due to the single breast compression of up to 10 min in duration. In the original pilot studies, in-house motion correction algorithms were applied to each image set before image subtraction.[18,19] In order to evaluate comparable levels of anatomical noise present upon radiologist interpretation, in this study a common motion correction algorithm was applied to the postcontrast images from both clinical pilot studies to register them to the precontrast images. An intensity-based multilevel image registration was performed using a MATLAB package, Flexible Algorithms for Image Registration (FAIR) written by Modersitzki.[44] In the image registration process, the images are first aligned using a 2D affine transformation. Then a deformable registration is performed using elastic regularization with the values $\alpha = 1000$, $\mu = 1$, and $\lambda = 0$, see Ref. 44 for more details. In both affine and deformable steps, a maximum of 25 iterations are chosen, sum of squared distance (SSD) is used as the dissimilarity measure, and spline interpolation is used to resample the intensity values on the new grid. A Gauss-Newton optimization scheme is employed for both the affine and deformable registration steps.

To test the effect of the image interpolation step of the motion correction algorithm on anatomical noise estimation, the power law parameters from the original and interpolated precontrast images were compared. Similarly, the effect of image registration on anatomical noise was assessed by a comparison of the power law parameters in the subtracted images with and without motion correction applied.

III.A.2. Image reading

The aim of this work is to evaluate anatomical noise contributed by normal breast tissue, which may affect the detection and characterization of lesions in CEDM images. Thus, regions of suspicious tissue must be identified for exclusion from power law analysis. The radiologists who had previously read the SE CEDM images for their respective pilot studies (R.A.J. and C.D.), each reread these images for anatomical noise analysis. The CEDM images were presented to the radiologists on a review workstation in a darkened room. The subtracted SE CEDM images at all time-points were made available along with the corresponding precontrast image for each case. The radiologists used either an ellipse tool or a polygonal region-of-interest (ROI) tool, which they were asked to place on the subtracted image at the time point with the greatest apparent extent of the suspicious region for CEDM images with enhancing lesions. The extent was determined in a subjective manner, based on the pattern of enhancement. If multiple suspicious regions existed, then multiple ROI were placed on the images, which could be chosen at different time points for identification of the maximum extent. In the case of no enhancement, the suspicious region identification was done on the precontrast mammogram. The coordinates of each ROI were recorded. If the lesion had been identified as out of the field of view for the CEDM exam at the initial reading, then no reading was required in this study. In all cases, the pathology reported lesion type and size, and radiographic findings of lesion morphology and localization from previous reads of the diagnostic DM and CEDM images were made available to the radiologists during the reading.

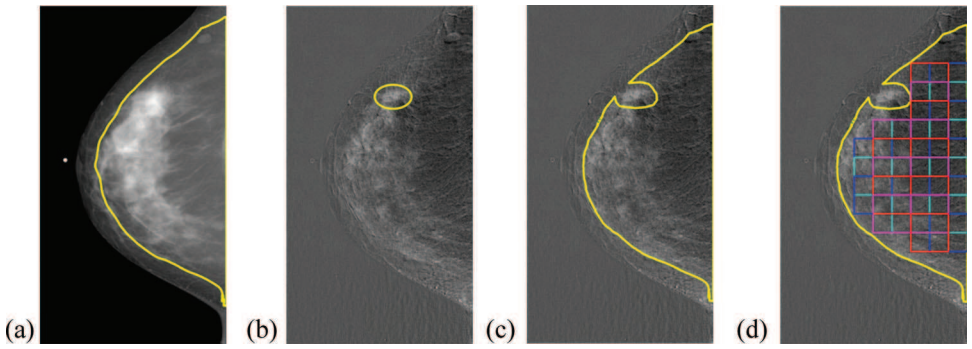

FIG. 2. (a) Constant thickness region identification; (b) suspicious abnormality segmentation; (c) mask region for spectral analysis; and (d) ROI selection.

III.B. Data preparation

All mammograms, from both DM and CEDM acquisitions, were converted to log-normalized intensities (LNI) for spectral analysis according to the relationship described by Mainprize *et al.*[45] Registered SE pre- and postcontrast CEDM images in LNI were subtracted according to Eq. (5).

III.B.1. Region selection

For each breast and view, a unique mask was generated to define the region for spectral analysis. Following the approach of Burgess, the first step of generating the mask was to identify the constant thickness region of the breast.[1] An area of approximately uniform thickness was found using a version of an algorithm introduced by Alonzo-Proulx *et al.*,[46] such that the region had 90% or greater of the maximum breast thickness. This is illustrated in Fig. 2(a). When visible, the pectoralis muscle was manually segmented from the images, and this region was removed from the constant thickness region. The final step of mask generation was to remove any areas that had been identified by a radiologist as containing a suspicious abnormality, such as in Fig. 2(b). This ensured that only apparently normal tissue remained in the region for spectral analysis, an example of which is demonstrated in Fig. 2(c). The same mask was applied to the precontrast image, each of the postcontrast images and the subtracted images since the breast remained under compression for the duration of the exam.

It is important to select a ROI size that is larger than most breast tissue structures to adequately sample the spatial frequency distribution of the tissue in the images. Human breast tissue is organized into 10–50 separate centimeter-scale lobes, each composed of a central lactiferous duct, with multiple terminal ductal lobular units (TDLU) branching off of this duct.[42] There are hundreds to thousands of TDLUs in the breast, normally sized between 1 and 8 mm, with most from 1 to 2 mm in diameter.[47] To capture the majority of these structures in the spectral analysis, ROI at a size of 256 × 256 pixels (25.6 mm on each side) were selected from within the masked area. This ROI size is also consistent with previously published anatomical noise investigations in mammography.[4,45]

Following the approach of Burgess, adjacent ROI were allowed to overlap by 50% in both the horizontal or vertical direction.[1] An example of the ROI extracted from one breast is illustrated in Fig. 2(d). Similar to the methodology of Engstrom *et al.*,[5] ROI that contained calcifications, or in some cases, lead markers, were excluded from analysis. To minimize the bias and variance in the WS estimates only mammograms with a minimum of four ROI were evaluated.[48] Across the 42 cases there were an average of 25 overlapped ROI selected per mammogram.

III.B.2. Power law analysis

III.B.2.a. Spectral measurement methods. The anatomical noise was determined from the ensemble average WS over all ROI from a mammogram in the manner described by Burgess.[1] The image WS was determined from the average of the squared magnitudes of the Fourier transform (FT) of an ensemble of M ROI as[49]

$$\mathrm{WS}(f_x f_y) = \frac{p_x p_y}{N_x N_y}\langle|\mathrm{FT}\{W_{xy}[\mathrm{ROI}(x,y) - \overline{I(\mathrm{ROI}_M)}]\}|^2\rangle, \tag{9}$$

where N and p are the ROI side length and pixel size in the x and y dimensions, respectively. The mean of the total region of image evaluation, which is defined as the area sampled by all M ROI, $\overline{I(\mathrm{ROI}_M)}$, is subtracted from each ROI. The units of the WS are expressed in mm^2. A Tukey window of the form, $W_{xy} = w(x)\,w(y)'$, was applied to reduce spectral leakage, where the window is defined as

$$w(x) = \begin{cases} \frac{1}{2}\left[1+\cos\left(\frac{2\pi}{r}\left(\frac{x-1}{N_x-1}-\frac{r}{2}\right)\right)\right] & 0 < \frac{x-1}{N_x-1} < \frac{r}{2} \\ 1 & \frac{r}{2} \le \frac{x-1}{N_x-1} < 1-\frac{r}{2} \\ \frac{1}{2}\left[1+\cos\left(\frac{2\pi}{r}\left(\frac{x-1}{N_x-1}-1+\frac{r}{2}\right)\right)\right] & 1-\frac{r}{2} \le \frac{x-1}{N_x-1} \le 1 \end{cases}, \tag{10}$$

with $r = 0.5$, for the N-point vectors x and y, from 1 to N_x and 1 to N_y, respectively. To restore the correct total WS after tapering, the Tukey window is normalized by multiplication with the factor, $\sqrt{\frac{N_x N_y}{\sum W_{jk}^2}}$.[50] In Eq. (9), subtraction of the mean over the total sampled image region, $\overline{I(\mathrm{ROI}_M)}$, is performed so that the integrated WS is a reasonable estimate of the variance of this image region. We note that the alternative approach of subtraction of the mean of each individual ROI, forces the zero frequency (dc) value of the WS to zero, thereby creating a "hole" in the spectrum (i.e., WS = 0 at $\rho = 0$ mm^{-1}). Convolution of the data taper with such a spectrum reduces the values of the WS at low frequencies.[1] This can potentially bias the power law parameter values, depending on the frequency interval used for the fit.

The ensemble average WS was found to be nearly isotropic and was converted to polar coordinates, WS(ρ, θ), to fit the data to a power law. The 2D FT of a real image has the property that it is complex conjugate-symmetric, WS(f_x, f_y) = WS*($-f_x$, $-f_y$), so the symmetric segments of the WS were discarded, and the remaining unique spectral components were sorted according to increasing radial frequency, ρ, to generate a 1D periodogram, WS(ρ). The power law parameters can then be determined from the solution to a weighted least squares fit[51] of the log-transformed data over a spatial frequency range, [ρ_l, ρ_u], in the form:

$$\log_{10}\{\mathrm{WS}(\rho_{[l,u]})\} = \log_{10}(\alpha) - \beta\log_{10}(\rho_{[l,u]}). \quad (11)$$

To ensure that β reflects the underlying anatomy rather than other contaminating noise sources, a range of spatial frequencies, [ρ_l, ρ_u], must be found where $\mathrm{WS_{An}} \gg \mathrm{WS_Q} + \mathrm{WS_{add}}$, in Eq. (7).

III.B.2.b. Frequency range for fit. In the literature there have been two general approaches for the selection of the frequency range for power-law fits to the WS. The first method is to select a fixed range over which the WS is generally dominated by the breast tissue variation, and to apply this to all cases under examination.[1,45] This approach can be robust when the relative contributions from anatomic noise and quantum and additive noise sources are reasonably constant between the images. The second approach, applied in situations where the relative contributions from the noise sources tend to fluctuate between cases, has been to vary the frequency range within some boundary frequencies, and to select a frequency range that corresponds to the best linear fit to the WS on a per-breast basis.[4,6] Recently, Mainprize *et al.* reported that lowering the high frequency limit for the linear fits increased the magnitude of the measured β.[45] For consistency of anatomical noise measurements between different breasts and between images of the same breast, we are convinced that, where possible, the same spatial frequency range should be applied for the power spectral analyses. However, this spatial frequency range must be carefully selected to ensure that the WS within that range reliably reflects the breast tissue properties among the different breasts and image types considered.

It is well known that low frequency artifacts are introduced to the WS by the image sampling window and the choice of the offset for subtraction from the ROI. Following the approach of other investigators, we have excluded the lowest sampled frequencies (0.0391–0.078 mm^{-1}) from our analysis to avoid these artifacts,[1–7] and applied a low frequency limit, ρ_l, of 0.08 mm^{-1} for all power law analyses. An additional reason that spectral measurements at spatial frequencies below 0.08 mm^{-1} are unreliable is that the lowest spatial frequency isotropically sampled within the flat-topped region of a 25.6 × 25.6 mm^2 Tukey window is 0.078 mm^{-1}.

The high frequency limit for spectral analysis, ρ_u, is less straightforward to determine. In conventional DM, it has been shown that for spatial frequencies greater than approximately 1.0 mm^{-1}, $\mathrm{WS_Q}$ dominates, so anatomical noise measurements are limited to spatial frequencies below this threshold.[1] The SE CEDM images are acquired with a HE x-ray beam, which results in a lower contrast between fibroglandular and adipose tissues as compared with typical DM energies.[39] The reduced contrast lowers the anatomical noise magnitude, such that for equivalent quantum and additive noise levels between DM and CEDM, the frequency at which quantum noise begins to dominate the WS shifts to lower spatial frequencies. Also, in the subtracted images, the contribution of stochastic noise from the two input images serves to increase the quantum noise power, further lowering the spatial frequency at which the quantum noise begins to dominate the WS in CEDM images. These effects were observed by Hu *et al.* in DE CEDM projection images, where an upper limit of 0.5 mm^{-1} was required for reliable power law analysis.[52]

In the SE CEDM studies evaluated, the exposures were selected to provide photon fluences at the detector for the HE exposure for CEDM that were equal to those used for a conventional DM exam of a breast of a given compressed thickness and proportion of fibroglandular tissue. Under these conditions, the relative contributions of quantum noise should be consistent between the unprocessed images. Thus, a fixed high frequency limit should be appropriate for spectral analysis of the HE images. To determine an appropriate high frequency limit, we take advantage of the multiple images acquired of the same breast under different conditions. As Hu *et al.* verified in projection images of a phantom,[52] and Vedantham *et al.* demonstrated with numerical simulations of breast CT,[53] the same value of β should occur in each image when a breast (without contrast agent) is imaged multiple times without repositioning between images, regardless of changes in imaging technique. Only the magnitude of the WS changes with the choice of x-ray beam. The precontrast SE CEDM images acquired with a HE beam should then be expected to have the same β as that of the WS for the same breast imaged under DM conditions. Thus, we aim to solve for the upper bound of spatial frequencies, ρ_u, which minimizes the difference between the power law exponents from the same breast imaged with DM and HE techniques, β_{DM}, and β_{HE}, respectively. By Eqs. (2), (7) and (9), for $\rho < \rho_u$ the WS of a log-normalized image can be written as

$$\mathrm{WS} = \frac{p_x p_y}{N_x N_y}|\mathrm{FT}\{W_{xy}[\Delta\mu_B(E)\theta(x,y)T - \Delta\mu_B(E)\overline{\theta(x,y)T}]\}|^2\mathrm{MTF}^2(E,f_x,f_y). \quad (12)$$

The apparent tissue structure, and consequently β, are dependent on the x-ray beam energy according to the system MTF in the following relationship:

$$\frac{1}{f^{\beta}} \propto |\mathrm{FT}\{W_{xy}[\theta(x,y) - \overline{\theta(x,y)}]\}|^2 \mathrm{MTF}^2(E, f_x, f_y). \tag{13}$$

Therefore, to measure the tissue structure in a manner that is independent of the particular imaging system, the influence of the system MTF should be corrected for by multiplication of the image WS by MTF^{-2}. After correction for the system MTF, the spatial frequency, ρ_u, which minimizes the difference $\beta_{DM} - \beta_{HE}$, can be determined from the following relationships:

$$\log_{10}\{\mathrm{WS}_{HE}\mathrm{MTF}_{HE}^{-2}\} = \log_{10}(\alpha_{HE}) - \beta_{HE}\log_{10}(\rho_{[l,u]}),$$
$$\log_{10}\{\mathrm{WS}_{DM}\mathrm{MTF}_{DM}^{-2}\} = \log_{10}(\alpha_{DM}) - \beta_{DM}\log_{10}(\rho_{[l,u]}), \tag{14}$$

where MTF_{DM} and MTF_{HE} are the system MTFs for the DM and HE x-ray beams, respectively.

For nine subjects in the Jong *et al*. dataset, sequential images were acquired under a single breast compression; first with a conventional DM technique and then a HE precontrast CEDM image.[18] These cases were used to measure the WS in the absence of a contrast agent under both DM and HE conditions, and to solve for ρ_u.

In the case of little patient motion and minimal contrast agent uptake in the breast, there can be a nearly complete cancellation of the tissue structure in the subtracted images, leaving only contributions from quantum and additive noise in the WS. In SE CEDM, this situation can occur at the earliest postcontrast time points, such as the case demonstrated in Fig. 3. Given the potential for variation in the amounts of contrast uptake and degrees of motion between subjects, as well as the increased quantum and additive noise components from combining two images, it was necessary to select the frequency range for power law analysis of SE subtracted images in a different manner than was used for the unprocessed images. For the SE subtracted images, the frequency range for power law fitting was determined on a per-breast basis by maximizing the correlation coefficient of the linear fit over a finite frequency range. For the first postcontrast time point in each series of subtracted images of a breast, the spatial frequencies were varied between boundaries of 0.16 mm^{-1} (min. 8 data points, e.g., Fig. 3), and the same upper limit for the spatial frequency range fit selected for the unprocessed images, ρ_u. To keep the spectral analysis consistent between the sequential images from a subject, the high frequency limit determined by this procedure, $\rho_{u,SE}$, was then applied to the anatomical noise analysis for the other subtracted images at later postcontrast injection time points.

The choices for the high frequency fitting limits were confirmed empirically. The level for the sum of quantum and additive noise, $\mathrm{WS}_Q + \mathrm{WS}_{add}$, was determined experimentally from an image of a uniform phantom (CIRS Inc., VA) with equivalent characteristics of thickness and attenuation to matched clinical cases. The intersection point of the WS of the uniform block and the breast image WS will then indicate the appropriate ρ_u. This was done for both the unprocessed images and subtracted images, with a correction for the system MTF applied to each uniform block and breast by multiplication of the image WS by MTF^{-2}. Attenuation properties of the block were matched according to the compressed breast thickness and the volumetric breast density (VBD) as estimated in DM images by Cumulus V, an in-house algorithm.[54] These images were also used to demonstrate the correlated signal component that is removed from the WS of SE subtracted images of a breast compared to a uniform object. Theoretical predictions of the subtracted image WS using Eq. (6), with and without the cross-correlation terms, were calculated and plotted together for the subtracted block and breast images. Equation (6) was verified for its accurate theoretical prediction by first calculating the subtracted image WS through appropriate summation of the WS of each input image and subtraction of the cross-correlation terms, and then comparing the result to a direct measurement of the WS from the SE subtracted images.

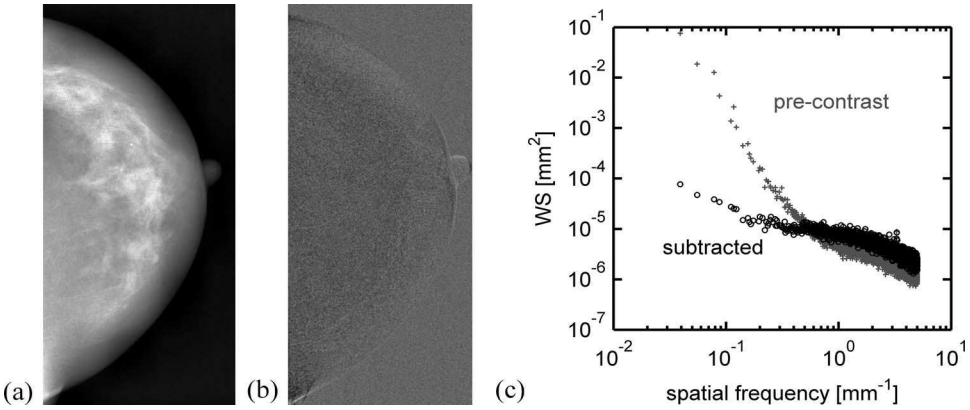

FIG. 3. An example SE CEDM case with minimal patient motion and contrast agent uptake at an early postcontrast injection time point. (a) Precontrast high-energy image (Mo/Cu, 41 kV, 140 mAs); (b) SE subtracted image at $t = 30$ s; (c) WS versus spatial frequency from the precontrast image in (a) (*gray* +), and the subtracted image in (b) (*black* ∘). Compared to the precontrast image WS, the WS for the subtracted image appears to have spectral content from breast tissue only to an upper limit, ρ_u, of between 0.1 and 0.2 mm^{-1}.

After confirmation of the suitable frequency range for power law fitting, the empirically derived frequency range, $[\rho_l, \rho_u]$, was applied for all anatomical noise analyses of the unprocessed images in this study. This same upper limit, ρ_u, was also used for spectral analysis of the SE subtracted images.

III.B.2.c. System MTF. The MTF for the HE x-ray beam is lower than that for the LE beam in the case of an indirect detector with a CsI phosphor because of k-fluorescence reabsorption in the phosphor as well as energy-dependent differences in the depth of photon interaction.[55] Additionally, the spatial distribution and relative proportion of x-ray scatter between DM and HE images changes according to the incident x-ray spectrum.[56] The effect of these factors on the WS can be estimated using a measurement of the system MTF with an appropriate scatterer in the x-ray beam. To determine the system MTF, an edge (400 μm-thick tantalum) ground to achieve a fine finish, was placed on top of 4.5 cm of poly(methyl methacrylate) (PMMA) at a slight angle ($\sim$3°) with respect to the chest wall edge of the breast support table.[57] The slanted edge was imaged under typical DM and HE conditions used in the SE CEDM studies (30 kV Rh/Rh and 46 kV Mo/Cu+Al) with a Senographe DS system (GE Healthcare, Chalfont St. Giles, UK), which is known to have nearly equivalent MTF as the Senographe 2000D over the frequency range of interest.[58] The system MTF measurement was repeated six times with each technique setting. The MTF tool was translated slightly ($<$1 mm) between each repeated exposure.

III.B.2.d. Anatomical noise magnitude. It follows from Eq. (12) that the anatomical noise magnitude is energy-dependent, and is proportional to the square of the differential linear attenuation coefficient between fibroglandular and adipose tissues,[59]

$$\alpha \propto \Delta\mu_B(E)^2 T^2. \tag{15}$$

For simplicity, we have presented Eq. (15) in an imaging system-independent form. Note that the system MTF will scale the magnitude of the WS in a frequency-dependent manner.

Using this x-ray energy-dependent relationship for α, the change in anatomical noise magnitude between DM and HE imaging techniques can be predicted by estimating $\Delta\mu_B$ for each spectrum. The effective linear attenuation coefficients for fibroglandular, μ_{fib}^{eff}, and adipose, $\mu_{adipose}^{eff}$, tissues, for an incident x-ray spectrum, $I_0(E)$, can be computed as follows:

$$\mu_m^{eff} = \frac{-1}{T}\log\left[\frac{\int_E I_0(E)\exp\{-\mu_m(E)\,T\}\,\eta(E)dE}{\int_E I_0(E)\eta(E)dE}\right], \tag{16}$$

where $\mu_m(E)$ is the linear attenuation coefficient for material, m, at photon energy, E, and the detector has an efficiency, $\eta(E)$. The polyenergetic spectra were generated using the spectral models published by Boone *et al.* with an extension of the Mo spectrum to 49 kV using the method implemented by Carton *et al.*[22,60] Attenuation from 0.275 cm thick polyethylene compression paddle and air of an appropriate thickness (source-to-detector distance – T) were included in the model of the incident x-ray spectrum. The filter thicknesses for the spectral models were calibrated using half-value layer measurements made on the clinical imaging system with high purity aluminum foils.

III.C. Data analysis

In this study, we evaluate the anatomical noise in multiple mammograms from the same subject, acquired at different time points or with different imaging techniques, or both. The utility of the power law model for linear fits to the WS for unprocessed and subtracted SE CEDM images was tested for significance using an F-test, and the Pearson correlation coefficient was computed for each fit. Incremental changes in the power law parameters for each woman between different imaging techniques and acquisition times were assessed to determine the influence of the imaging condition on the observed anatomical noise. A paired Student's t-test was applied to determine statistical significance of the differences between the repeated measures. To compare anatomical noise parameters between the different study cohorts examined, the independent population metrics were compared with a two-sample Student's t-test.

Trends in the power law parameters as a function of time after contrast administration in the SE CEDM images were evaluated by fitting models to the data to explain the functional relationships. When no statistical difference was found between anatomical noise measurements from the Dromain *et al.* and Jong *et al.* cases, the results were pooled for analysis. Because unequal numbers of cases were evaluated in each study, and the patient populations had different characteristics, unequal standard deviations arise at each time point. To account for these variations in the spread of data, weighted least squares regression was used for the fitting. The utility of each model was tested for significance using an F-test. A significance level of 0.05 was used for all statistical tests in this work.

IV. RESULTS

IV.A. Power law analysis methods

The system MTFs measured for DM and HE imaging conditions are shown in Fig. 4. Based on the uncertainty in the system MTF from the six repeated measurements, it was found that the MTFs at each technique setting were significantly different. For each of the nine cases in the SE CEDM dataset with DM and CEDM images acquired during the same breast compression, a correction factor of MTF^{-2} was applied to the WS calculated for the DM and HE images, respectively. With this correction applied, β was estimated from a linear fit between a lower bound of 0.08 mm^{-1}, and an upper bound from 0.2 to 0.8 mm^{-1}. Comparing measurements of β_{DM} and β_{HE} for the same breast, it was determined that the difference, $\beta_{DM} - \beta_{HE}$, was minimized with a high frequency limit of 0.30 mm^{-1} ($\beta_{DM} - \beta_{HE} = 0.002$).

The system MTF correction of the HE images decreased the mean β by 0.098 ($p \ll 0.05$), and increased α by 5.7 $\times$ 10^{-7} mm^2 ($p \ll 0.05$), while MTF correction of the WS of the DM images decreased the average β by 0.05 ($p \ll 0.05$)

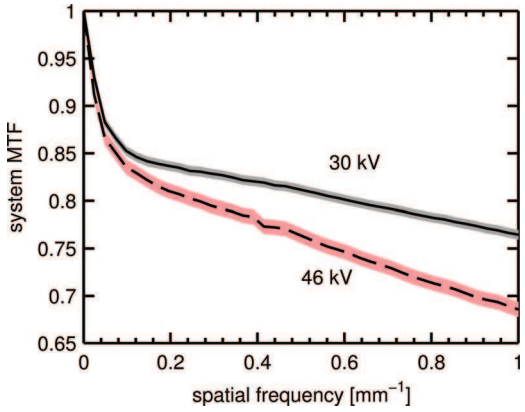

FIG. 4. A plot of the system MTF for the Senographe DS under the imaging conditions used for the SE CEDM studies, with 4.5 cm of PMMA in the beam at typical low-energy (Rh/Rh 30 kV, *solid line*) and high-energy (Mo/Cu+Al 46 kV, *dashed line*) technique settings. The curves each represent the mean of six repeated measurements of the system MTF, with the 95% confidence intervals indicated by the shaded regions. The spatial frequency range of interest for power law analysis was less than 1 mm^{-1}.

and increased the α values by 8.8×10^{-6} mm^2 ($p \ll 0.05$). Prior to the system MTF correction there was a nonsignificant mean difference between β_{DM} and β_{HE} for the nine women of 0.04 ($p = 0.43$), which the MTF correction reduced to 0.002 ($p = 0.97$). Figure 5 illustrates the effect of the MTF correction for an example case, where the WS and the associated power law parameters are shown prior to MTF correction in (a), and after the MTF correction in (b). The MTF correction was applied for all power law analyses described below to estimate the intrinsic tissue WS in an image.

Without a data taper applied, there are often strong artifacts along and near the axes ($f_x = 0$ and $f_y = 0$) of the 2D WS due to the spectral leakage that arises from discontinuities in signal at the edges of the ROI. These artifacts were greatly reduced by the application of the Tukey window to taper the signal at the ROI edges to zero. A test of the sensitivity of the measurement of the anatomical noise parameters to the use of the Tukey window was performed using the 20 cases from the Dromain *et al*. study. A comparison of these parameters with and without the window applied as defined in Eq. (10), shows that for both unprocessed images and subtracted images, each of α and β changed to a statistically significant degree. Compared to the WS from the untapered ROI, in the unprocessed and SE subtracted images, respectively, the use of a Tukey window resulted in decreases in α of 53% and 27% relative to the untapered case, and average absolute increases in β of 0.34 and 0.15 ($p \ll 0.05$). The changes in α and β observed when the Tukey window was used appeared to be due to a restoration of spectral leakage to the appropriate spatial frequencies in the WS.

The spatial frequency at which quantum noise begins to dominate the WS for the images evaluated in this work was also determined empirically. Images were acquired of a uniform block of breast tissue-equivalent plastic of the same thickness and x-ray attenuation as several corresponding clinical cases. These images were acquired on the same mammography system and with identical technique factors to match the levels of quantum and electronic noise present in the clinical images. The source images and the associated WS for a representative SE CEDM clinical case, and a corresponding uniform block are shown in Fig. 6.

Based on an evaluation of the lowest spatial frequency where the breast WS intersects with the block WS for a number of SE cases, it was confirmed that a spatial frequency upper bound, ρ_u, of 0.30 mm^{-1} for the linear fitting region ensures that the portion of the WS evaluated for power law analysis is not dominated by quantum noise. The spatial frequency range of 0.08–0.30 mm^{-1}, was implemented for linear fits to the WS for all subsequent power law analyses of unprocessed images in this work.

For the SE subtracted images, the upper spatial frequency limit was determined on a per-breast basis, as that which maximized the correlation coefficient for fits to the WS. On

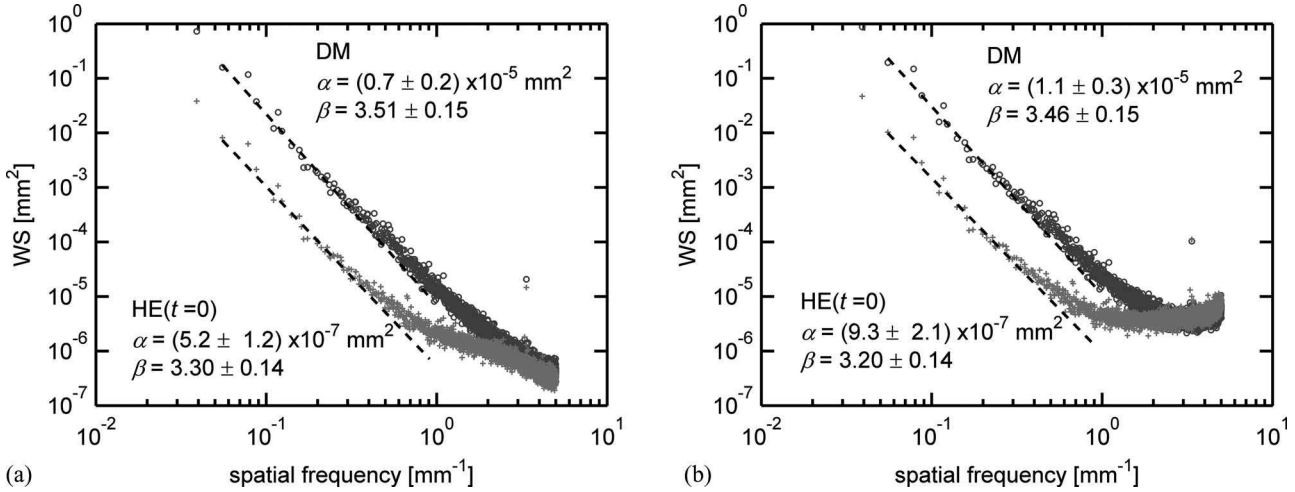

FIG. 5. An illustration of the x-ray spectral energy response of the image WS, and the effect of a correction for the system MTF under DM and HE image technique settings. (a) The system-dependent image WS for DM (Rh/Rh 32 kV, 180 mAs) and precontrast HE (Mo/Cu 49 kV, 180 mAs) images of the same breast and the power law parameters from fits to these WS (from 0.08 to 0.30 mm^{-1}). (b) The same spectra as plotted in (a) after correction for system MTF, and their associated power law parameters.

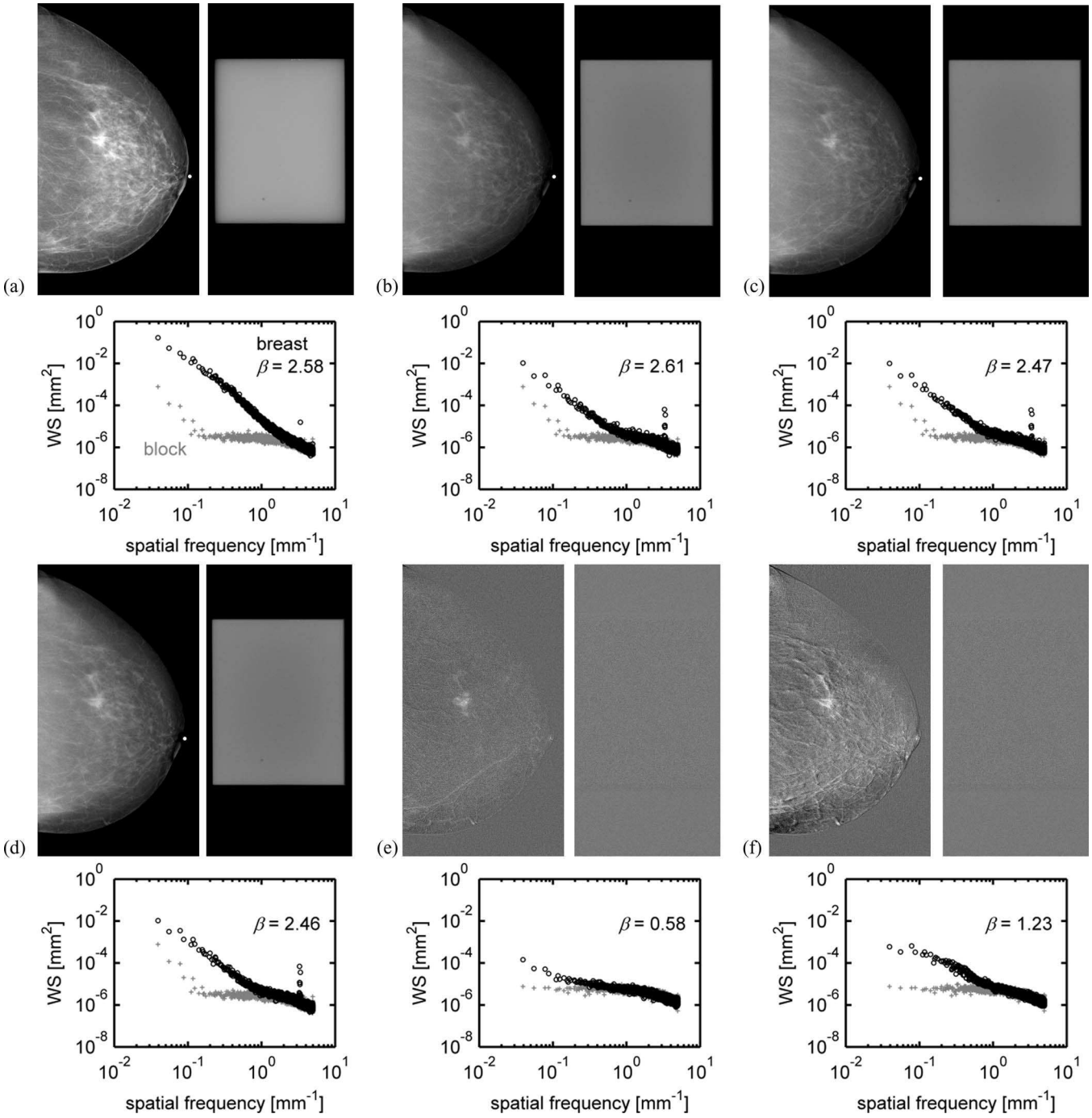

FIG. 6. SE CEDM images and corresponding WS for a representative clinical case (*black* ∘) and a uniform phantom (*gray* +) with matched imaging conditions for (a) conventional DM (Mo/Rh, 28 kV, 80 mAs); (b) a precontrast image (Mo/Cu, 45 kV, 90 mAs); (c) postcontrast image at 1 min; (d) postcontrast image at 10 min; (e) SE subtracted image at 1 min; and (f) SE subtracted image at 10 min. Values of β calculated from the breast images are shown. The volumetric breast density was estimated as 8% (Ref. 54) and the compressed breast thickness was 47 mm. To simulate these properties, plastic blocks were imaged with x-ray attenuation equivalent to 1 cm of 50/50 fibroglandular/adipose by weight and 4 cm of adipose (CIRS Inc., VA). For simplicity of interpretation, all WS plotted in this figure were measured from the original images (no interpolation), and are presented without system MTF correction.

average, the upper spatial frequency limit for fits to the WS of the subtracted images was 0.25 mm^{-1}. Subjectively, this limit appeared to be appropriate, given the smaller contribution from breast tissue structure in the WS of the subtracted images, which is only apparent at the lowest frequencies as seen in Figs. 3(c) and 6(e).

Figure 7 illustrates the correlated signal component that is removed from the WS by SE image subtraction for an example clinical case and corresponding uniform block images. For both sets of images the WS_{SE} was calculated by Eq. (6) and is plotted with and without the cross-correlation terms. Note that no significant difference was found between the

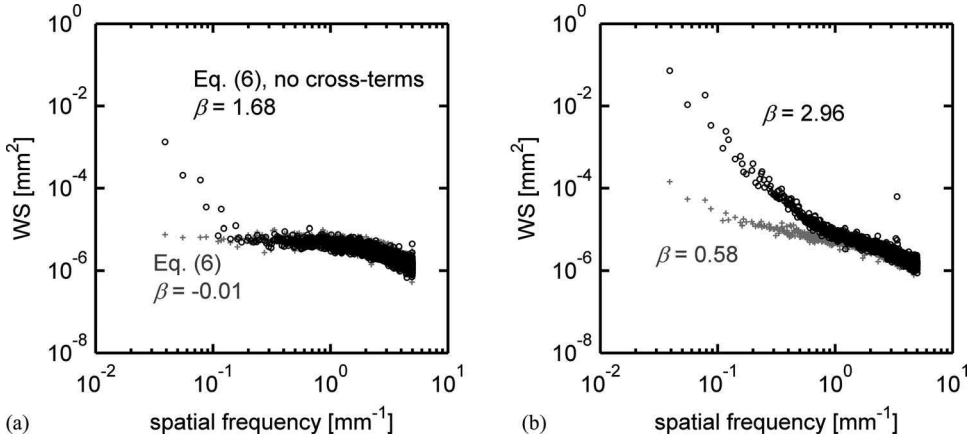

FIG. 7. The SE subtracted CEDM image WS as predicted by Eq. (6), with (*gray* +) and without (*black* ○) the cross-correlation terms included, and the associated measured β. The difference between the WS demonstrates the power in the correlated component of the signal between the precontrast and postcontrast images for (a) a uniform block, and (b) the breast considered in Fig. 6 at 1 min postcontrast administration. For simplicity of interpretation, all WS plotted in this Figure were measured from the original images (no interpolation), and are presented without system MTF correction.

anatomical noise parameters measured from SE subtracted image WS or the theoretical prediction of WS_{SE} based on the full implementation of Eq. (6).

IV.B. SE CEDM anatomical noise

IV.B.1. Image registration

The motion correction algorithm applied in this work uses a pyramid decomposition scheme where the images are resampled using spline interpolation, first to lower resolutions for initial estimation of the image transformation parameters before ultimately upsampling a registered image to the original resolution after several iterations. It is well known that resampling an image can result in an effective loss of resolution. Power law analysis of the precontrast images (no motion correction) from the Jong *et al*. SE CEDM dataset was done with and without image interpolation. As shown in Fig. 8, image interpolation strongly reduces the WS at high spatial frequencies (>1 mm^{-1}), but the effect was negligible over the frequency range of interest for anatomical noise evaluation. No significant differences were found in α ($p = 0.64$) or β ($p = 0.47$), as measured from the WS of the original and interpolated precontrast images.

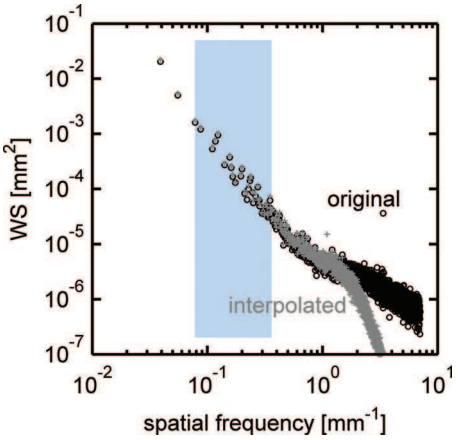

FIG. 8. Influence of image interpolation on the WS of the precontrast image shown in Fig. 6(b). No appreciable difference exists between the WS of the original (*black* ○) and interpolated image (*gray* +) over the spatial frequencies of interest for power law analysis (*shaded region*).

Examples of subtracted CEDM images with and without motion correction applied are shown in Fig. 9. Motion correction resulted in no significant change in α in the subtracted images ($p = 0.59$) compared to the uncorrected images. In the subtracted images, β was significantly lower ($p < 0.05$) after motion correction by an average of 0.13 among the 42 subjects, and over all times postcontrast.

IV.B.2. Power law parameters

Power law analysis was applied to the SE CEDM images at each time point for both the unprocessed images and the SE subtracted images. The results from assessment of 20 cases from the Dromain *et al*. study are summarized in Table I, and the results from 22 cases from the Jong *et al*. study dataset are compiled in Table II. The power law parameters summarized in Tables I and II represent the intrinsic tissue anatomical noise because the WS were each corrected for the system MTF. For reference purposes we have also included the system-dependent power law parameters (no MTF correction) for each of the clinical image datasets in the Appendix in Tables IV and V. All linear fits to the WS were significant, with Pearson correlation coefficients of 0.98 ± 0.01 in the unprocessed images and 0.92 ± 0.06 in the SE subtracted images. The between-subject variability was larger than the uncertainties in the parameters for an individual breast, so the standard deviations of the power law parameters among the subjects are reported in the tables. The standard errors of the power law parameters due to uncertainty of the model fit to an individual image WS were an average of about 22% of α and 5% of β for the unprocessed images, and were larger for the subtracted images, at about 29% of α and 11% of β.

The results in Tables I and II were evaluated for a relationship between anatomical noise and the time distribution of the contrast agent. Figure 10 illustrates a comparison of

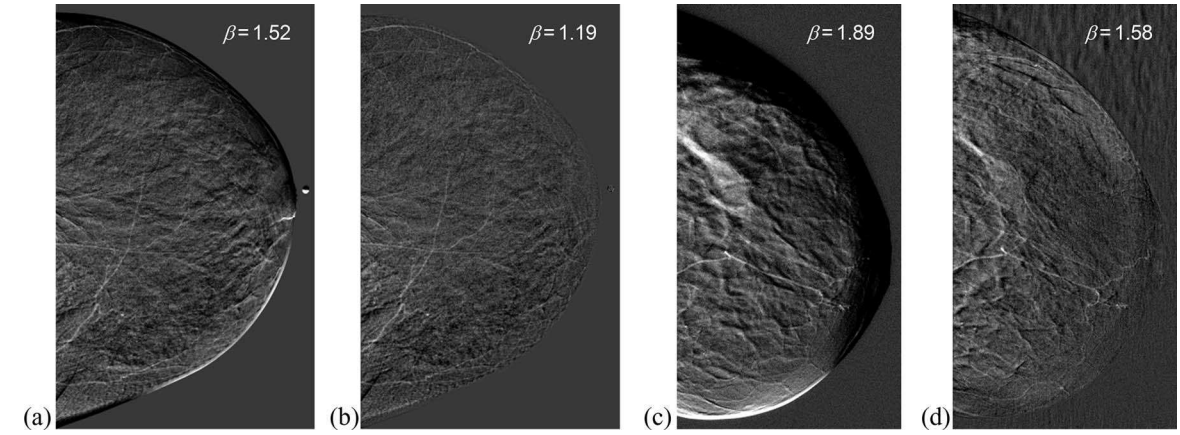

FIG. 9. Log-subtracted SE CEDM images and the associated power law exponent, β, of the normal tissue. Images (a) and (c) have no motion correction applied, while (b) and (d) were aligned with nonrigid registration. The images are displayed with the same window and level settings.

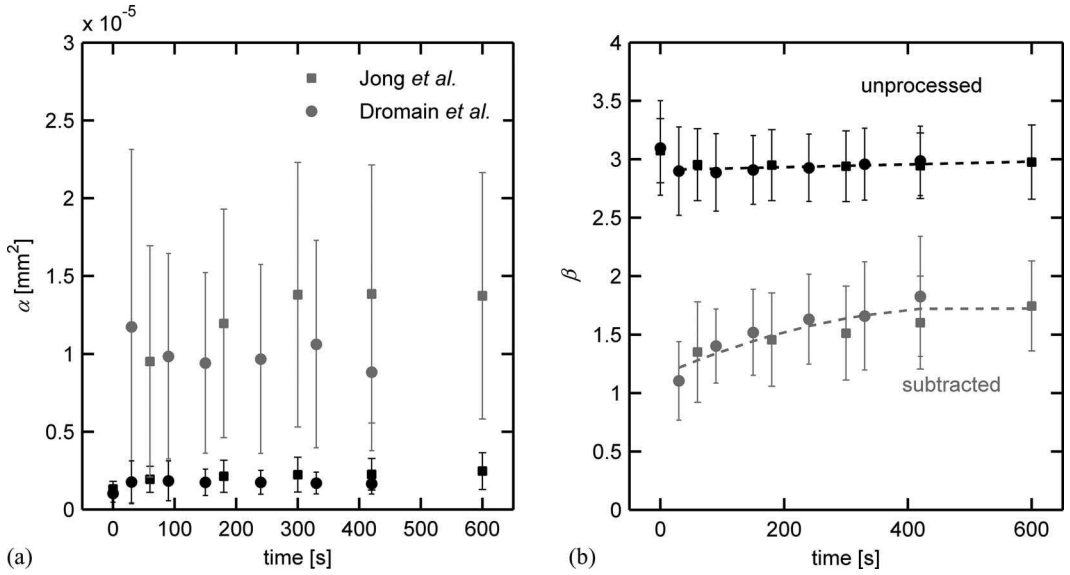

FIG. 10. Power law parameter time-dependence analysis results for SE CEDM images; (a) α, and (b) β in unprocessed (*black*) and subtracted images (*gray*) versus time after contrast agent injection as measured from each dataset (Jong = ■, Dromain = ●), with error bars that denote the standard deviation of the data. The dashed lines are weighted least squares fits to the combined datasets. No significant fits were found to α from the unprocessed images or the subtracted images.

TABLE I. Dromain *et al*. study SE CEDM power law analysis results from 20 cases.

	Unprocessed				SE subtracted			
Time (s)	$\bar{\beta}$	$\sigma(\beta)$	$\bar{\alpha}$ (mm^2)	$\sigma(\alpha)$	$\bar{\beta}$	$\sigma(\beta)$	$\bar{\alpha}$ (mm^2)	$\sigma(\alpha)$
0	3.10	0.41	1.0×10^{-6}	0.6×10^{-6}	N/A		N/A	
30	2.90	0.38	1.8×10^{-6}	1.4×10^{-6}	1.10	0.34	1.2×10^{-5}	1.1×10^{-5}
90	2.89	0.33	1.8×10^{-6}	1.3×10^{-6}	1.40	0.32	1.0×10^{-5}	0.7×10^{-5}
150	2.91	0.29	1.7×10^{-6}	0.9×10^{-6}	1.52	0.37	0.9×10^{-5}	0.6×10^{-5}
240	2.93	0.29	1.7×10^{-6}	0.8×10^{-6}	1.63	0.38	1.0×10^{-5}	0.6×10^{-5}
330	2.96	0.31	1.7×10^{-6}	0.7×10^{-6}	1.66	0.46	1.1×10^{-5}	0.7×10^{-5}
420	2.99	0.30	1.7×10^{-6}	0.67×10^{-6}	1.83	0.51	0.9×10^{-5}	0.5×10^{-5}

TABLE II. Jong *et al.* study SE CEDM power law analysis results from 22 cases.

	Unprocessed				SE subtracted			
Time (s)	$\bar{\beta}$	$\sigma(\beta)$	$\bar{\alpha}$ (mm^2)	$\sigma(\alpha)$	$\bar{\beta}$	$\sigma(\beta)$	$\bar{\alpha}$ (mm^2)	$\sigma(\alpha)$
0	3.10	0.27	1.3×10^{-6}	0.5×10^{-6}	N/A		N/A	
60	2.95	0.31	1.9×10^{-6}	0.8×10^{-6}	1.35	0.43	1.0×10^{-5}	0.7×10^{-5}
180	2.95	0.30	2.1×10^{-6}	1.0×10^{-6}	1.46	0.40	1.2×10^{-5}	0.7×10^{-5}
300	2.94	0.30	2.2×10^{-6}	1.1×10^{-6}	1.51	0.40	1.4×10^{-5}	0.8×10^{-5}
420	2.94	0.28	2.3×10^{-6}	1.0×10^{-6}	1.60	0.40	1.4×10^{-5}	0.8×10^{-5}
600	2.98	0.32	2.5×10^{-6}	1.2×10^{-6}	1.75	0.38	1.4×10^{-5}	0.8×10^{-5}

the results from these two studies, plotting the data together as a function of image acquisition time postcontrast injection, with error bars that represent the standard deviation among the women. A two-sample Student's *t*-test could not distinguish the α and β parameters at coincident time points (i.e., $t = 0$ and 420 s, $p > 0.05$) from the Dromain *et al.* and Jong *et al.* studies. Therefore, data for the images with contrast agent present from the two trials were pooled and weighted least squares regressions were made to each parameter as a function of time after contrast agent injection. Polynomial and exponential functions were tested for the significance of their fit to the data. A linear fit to β versus time from unprocessed images with iodine present ($t > 0$ s) proved significant ($F = 9$, $p = 0.02$), with a functional form of $\beta_{HE}(t) = 1.19 \times 10^{-4} t + 2.91$, and $R^2 = 0.52$. The quadratic, $\beta_{SE}(t) = -1.31 \times 10^{-8} t^2 + 1.27 \times 10^{-4} t + 1.05$, provided a significant fit ($F = 21$, $p = 0.001$) to the SE subtracted image β as a function of time with a coefficient of multiple determination, R^2, of 0.86. These fits are shown as dashed lines in Fig. 10(b). No significant relationships were found between α and the time after contrast injection as measured in either the unprocessed or subtracted images.

In a subset of nine subjects from the Jong *et al.* dataset, conventional, noncontrast, DM were acquired immediately (~1 min) before the CEDM exam, under the same breast compression. The results of the measurements of the power law parameters α and β on this subset of cases are listed in Table III. The mean of the distribution of β differences, $\beta_{DM} - \beta_{t0}$, of −0.002, cannot be distinguished from zero ($p = 0.97$), while the magnitude of α in the DM images is significantly larger than for the precontrast image at $t = 0$ s by 2.3×10^{-5} mm^2 ($p \ll 0.05$).

V. DISCUSSION

V.A. Power law analysis of CEDM images

Although power law analysis has been used previously to model the anatomical noise in mammographic imaging, including conventional mammography, tomosynthesis, and breast CT,[2–6,8,45] this is the first study to apply a power law to characterize anatomical noise in CEDM clinical images. The signal changes introduced by the contrast agent in CEDM are small relative to the native breast tissue contrast, usually resulting in less than a 5% increase in x-ray attenuation.[61] Given these small signal fluctuations it is reasonable to assume that the anatomical noise in the unprocessed images, will also exhibit power-law behavior. However, the procedure of image subtraction in CEDM largely cancels the breast tissue signal, leaving residual signal due to contrast agent uptake in the tissues. Hence, the validity of the power law as a model for anatomical noise in the CEDM subtracted images requires assessment.

Figure 7 illustrates how the log-subtraction process removes some of the correlated signal between the precontrast and postcontrast images. In the unprocessed block images, the signal is nonuniform across the image due to the presence of shading artifacts caused by scattered radiation. This nonuniformity contributes power in the image WS at low frequencies, as demonstrated by the gray WS curve from the uniform block image in Fig. 6(a). This artifact is present in both the representative "precontrast" and "postcontrast" images of the block (both block images were acquired with no contrast agent), so these correlated signals are eliminated in the subtracted image, as seen in the gray WS in Fig. 7(a), which approaches a slope of zero at the lowest spatial

TABLE III. Jong *et al.* study SE CEDM results from nine cases with DM.

	Digital mammogram				CEDM unprocessed				SE subtracted			
Time (s)	$\bar{\beta}$	$\sigma(\beta)$	$\bar{\alpha}$ (mm^2)	$\sigma(\alpha)$	$\bar{\beta}$	$\sigma(\beta)$	$\bar{\alpha}$ (mm^2)	$\sigma(\alpha)$	$\bar{\beta}$	$\sigma(\beta)$	$\bar{\alpha}$ (mm^2)	$\sigma(\alpha)$
0	3.06	0.36	2.5×10^{-5}	1.5×10^{-5}	3.06	0.34	1.3×10^{-6}	0.7×10^{-6}	N/A		N/A	
60	N/A		N/A		2.96	0.37	1.9×10^{-6}	1.0×10^{-6}	1.33	0.36	0.7×10^{-5}	0.6×10^{-5}
180	N/A		N/A		2.97	0.38	2.1×10^{-6}	1.4×10^{-6}	1.59	0.44	0.7×10^{-5}	0.5×10^{-5}
300	N/A		N/A		2.98	0.38	2.2×10^{-6}	1.4×10^{-6}	1.68	0.39	1.0×10^{-5}	0.9×10^{-5}
420	N/A		N/A		2.97	0.33	2.2×10^{-6}	1.3×10^{-6}	1.72	0.40	1.1×10^{-5}	0.8×10^{-5}
600	N/A		N/A		2.95	0.42	2.7×10^{-6}	1.6×10^{-6}	1.72	0.36	1.3×10^{-5}	0.8×10^{-5}

frequencies. For identical breast parenchymal patterns, the WS from subtracted SE breast images should ideally also have a slope close to zero at low spatial frequencies. However, in the subtracted breast image WS compared to that of the uniform block WS, some noise power due to residual tissue structure remains. This is illustrated in Figs. 3(c), 6(e), and 6(f). These residual patterns in the SE subtracted images cause the WS to have a nonzero slope at low spatial frequencies, even when motion artifact is minimal, as in Figs. 3 and 6(e). This observation led to our hypothesis that the presence of the contrast agent in the breast in a nonuniform distribution, as suggested in Eq. (4), has an influence on the anatomical noise in CEDM, and demonstrates the need for the residual anatomical noise term, WS_{An}^{SE}, in Eq. (8).

In this work, we model the residual anatomical noise in SE subtracted images with the power law in Eq. (1). In all cases, an *F*-test found the linear fits to the WS data in log-log space to be significant ($p \ll 0.05$). Therefore, a power law was empirically determined to be a reasonable model for the anatomical noise in CEDM. The Pearson correlation coefficient was found to be 0.98 in the SE CEDM unprocessed images, however, the correlation reduced slightly, to about 0.92, in the subtracted images. It is likely that the additional quantum noise present in the subtracted images, the presence of motion artifact, and the shorter frequency range for the power law fitting (0.08 mm^{-1} to ~0.25 mm^{-1} vs 0.30 mm^{-1}) are each partially responsible for the weaker correlations.

V.B. X-ray spectrum

Although β does not change with the x-ray spectrum energy, the magnitude of α does, as demonstrated in Fig. 5 and by the energy-dependence in Eq. (15). The WS of the image in LNI will vary linearly with the square of the differential linear attenuation coefficient, $\Delta\mu_B$. Thus, using the average subject characteristics and imaging techniques among the nine CEDM cases with DM, we can predict that for a 6.0 cm compressed breast imaged with a 30 kV Rh/Rh DM beam, and a 46 kV Mo/Cu+Al HE beam, the effective differential linear attenuation coefficients, $\Delta\mu_B$, will change from about 0.29 cm^{-1} to 0.07 cm^{-1}.[39,60] Thus, with all else held constant, the WS magnitude of the HE image should be smaller than that in the DM image by a factor of just greater than 17 $[(\Delta\mu_B^{DM}/\Delta\mu_B^{HE})^2 \approx 17.2]$. This prediction is in agreement with our measurements of α for the DM (2.5×10^{-5} mm^2) and HE (1.3×10^{-6} mm^2) images (see Table III) that have a ratio of 18.7 ± 2.4.

This lower anatomical noise magnitude with a HE beam also affects the upper limit of the spatial frequency range that reliably contains information on the breast tissue structure. Compared to DM, the WS due to breast tissue structure is shifted the downwards, moving the intersection point of the WS from the tissue and that from stochastic noise to lower spatial frequencies. Furthermore, in the subtracted images, the addition of noise from two input images increases the quantum noise component. These two effects led to the selection of a narrow spatial frequency range for power law analysis with a maximum of 0.30 mm^{-1}, so that consistent power law fits could be made for each image type with a minimal influence from stochastic noise.

The average β of 3.08 ± 0.34, measured among the 42 SE CEDM images at $t = 0$ s (no contrast agent) over the selected spatial frequency range, 0.08–0.30 mm^{-1}, demonstrates good agreement with others who have measured β to be in the range of 2.8–3.1 in mammograms.[4,5,8,45] The anatomical noise magnitude is not reported as often in the literature since it is strongly dependent on the imaging technique [see Eq. (15)]. However, the value of α in the DM images of 2.5×10^{-5} mm^2 is in good agreement with recent reports in the literature of α measured in DM images acquired with similar mammography systems.[45] The small decrease in β of 0.05 after correction of the DM image WS for the system MTF is on the same order as that reported by Mainprize *et al.*, at 0.08, after comparable MTF compensation.[45]

V.C. Presence of contrast agent

As described above, image subtraction is applied in CEDM because the signal changes introduced by the contrast agent are small relative to the native breast tissue contrast. One might then presume that the anatomical noise in the unprocessed postcontrast images would remain relatively unchanged compared to the precontrast images. Although the impact of the contrast agent is small relative to the standard deviation in the parameters between women (see Fig. 10), the change in the anatomical noise in the SE CEDM postcontrast images compared to the precontrast images is measureable when the differences in anatomical nose parameters for a single breast are evaluated. From the data presented in Tables I and II, the introduction of contrast agent resulted in a significant increases in α of 7.4×10^{-7} mm^2 and 6.3×10^{-7} mm^2 ($p \ll 0.05$), and significant decreases in β of 0.20 and 0.12 ($p \ll 0.05$), between the precontrast image and the first postcontrast image in the Dromain *et al.* and Jong *et al.* studies, respectively. In the unprocessed images, the anatomical noise magnitude, α, remained significantly larger at all postinjection time points compared to the power law parameters in the precontrast images ($p \ll 0.05$). While the increase in the anatomical noise magnitude with contrast agent injection is relatively large, at about 50% of the precontrast value, the decrease in β is only about 5% of that in the precontrast images. To understand the source of the change in the anatomical noise structure with contrast agent, it is more instructive to evaluate the subtracted SE CEDM images. In these images, the contrast agent is likely the predominant source of the image signal, and β is observed to vary strongly with the timing of the image acquisition.

V.D. Timing of CEDM imaging

There are several factors to consider in the timing of a CEDM exam. First, one would like to make image acquisitions at a time point that captures the greatest lesion-to-background signal ratio to maximize lesion detectability. Second, to gain functional information about a lesion, enough time points must be sampled to provide adequate contrast

agent wash-in and wash-out characteristics. Third, while balancing the desire to obtain contrast agent kinetic information, it is also desirable to keep the total exam duration short to minimize the potential for motion artifacts. In our analysis here, we evaluate the time-dependence of the anatomical noise, which might help inform the design of a clinical image acquisition protocol to meet some of the criteria above.

An analysis of the anatomical noise in the unprocessed images versus postinjection time reveals information about the contrast agent distribution between the VS and EES tissue compartments. It is well known that a state of equilibrium for the contrast agent concentration between the VS and EES is typically reached within 3–5 min depending on the injection protocol and patient characteristics.[62,63] It is likely that for the SE CEDM studies evaluated here, that equilibrium of the contrast agent between the VS and EES had been reached by about 5 min postcontrast. We hypothesize that prior to the 5 min time point, a greater proportion of contrast agent in the VS compared to the EES contributes to a high contrast of blood vessels in the image. These high-contrast structures would produce a corresponding large power in the WS at the high end of the spatial frequency range compared to a precontrast image, thereby reducing the WS slope, and consequently, β.

In SE subtracted images the breast tissue signal is predominantly removed by image subtraction, so β in these images should then be a more direct measurement of the contrast agent distribution structure than in the unprocessed images. Given our hypothesis that β is lowest in the vascular phase of contrast agent distribution, β would be expected to increase with time postcontrast. Indeed, as shown in Fig. 10(b) (*gray* markers), the magnitude of β for the subtracted images increases with time, and begins to plateau at about 300 s, which is consistent with the premise that equilibrium may have been reached between the contrast agent in the VS and in the EES around this time.

Although a motion correction algorithm was applied prior to measurement of the WS in this study, it is clear from the appearance of some of the subtracted images after registration, such as in Fig. 9(d), that the motion correction is not perfect. Therefore, the WS of SE subtracted images may have some contribution from motion artifact as well as that due to contrast agent distribution in the breast tissue.[64] This artifact can be especially pronounced in SE subtracted images of later postcontrast time points, and is readily apparent in Fig. 6(f). In this work, we do not separate the effects, but rather we measure the WS in the subtracted images as they are presented to a radiologist for review (i.e., after motion correction) to capture the total anatomical noise that may interfere with image interpretation. Thus, what is likely a motion artifact that increases with time postcontrast, partially contributes to the observed quadratic relationship of β with time as plotted in Fig. 10(b).

V.E. CEDM performance

Recently, there has been interest in calculating the power law exponent, β, in mammographic backgrounds.[4–6] This work is largely motivated by the observations of Burgess *et al.* that for power law backgrounds with similar α, lesions will be detectable at smaller sizes in mammograms, or mammogram regions, with smaller β.[8] This finding is applicable to projection images where the lesion signal amplitude is proportional to its linear attenuation integrated over its thickness. Similarly, the literature suggests that for a constant lesion signal, a reduced α will result in greater lesion detectability.[11,12] Although further investigations of the relationships between anatomical noise parameters and lesion detection are required in each modality under consideration, these results imply that a decreased anatomical noise could lead to increased detection performance.

In CEDM, we have found that logarithmic subtraction results in images with reduced β compared to DM and unprocessed CEDM images. Also, α is a factor of 2 smaller in the subtracted images than in DM images. Although the reduction in these anatomical noise parameters suggests that there may be improved lesion detectability in CEDM backgrounds compared to DM, we caution that the data presented here do not test this hypothesis. Information about the lesion signal has not been considered in this work, which must be evaluated to determine the relative detectability between CEDM images and conventional DM. Some preliminary work on this subject from our group suggests that lesion detection is indeed improved in CEDM compared to DM,[65] but this is an area of ongoing research. Future work will involve characterization of lesion signal in CEDM to confirm the detectability relationships.

Apart from sensitive lesion detection, an important contribution of CEDM may be the information on tumor angiogenesis that can be obtained through lesion signal enhancement levels, contrast agent kinetics, tumor morphology, or a combination of these factors.[18–20] Anatomical noise in CEDM may affect the interpretation of these parameters, however, recent results on the enhancement of the normal parenchyma in breast MRI suggest that the magnitude of the contrast agent uptake in the normal breast tissue in CEDM could potentially also carry diagnostic information. In breast MRI it has been reported that greater contrast agent uptake in the normal breast tissue is associated with a greater odds of breast cancer.[24] Therefore, the relationships between the anatomical noise in CEDM and lesion characterization, and the presence of a cancerous lesion will be important areas of future work using these metrics.

This study characterized the anatomical noise in SE CEDM from images acquired in two independent clinical pilot studies.[18,19] Although the mammography systems and the technique factors used for the image acquisitions were nearly identical between the trials, the injection protocols and the timing of postcontrast image acquisition differed as depicted in Fig. 1. As shown in Fig. 10, the anatomical noise measurements were consistent among the two cohorts of women, including the results as a function of postinjection time. At equal image acquisition time points, no statistically significant difference was found between the two groups, and over time postcontrast, the results followed a global trend. Thus, we find that the anatomical noise in CEDM images is not strongly dependent on the injection protocol, and that the

noise characteristics have a predictable relationship with the time postcontrast administration. These robust results suggest that prognostic estimates of the anatomical noise parameters can be reliably made to evaluate, and to potentially compare, CEDM system performances.

V.F. Study limitations

The description of CEDM anatomical noise as a power law relies on stationarity of the WS, which is an approximation for breast tissue. It is well known that breast structure varies regionally, and so individually, each ROI has a WS that is unique and may be nonisotropic.[7] Taking the ensemble average WS across all ROI largely eliminates radial asymmetry, and the measured power law parameters should reflect the average tissue and not represent the regional structures of the breast. The regional variations in structure that were not captured in this analysis might be important as a diagnostic indicator of tissue distortions caused by the presence of cancer that can appear as asymmetries compared to the contralateral breast, and also may be important for lesion detection and characterization within a background that has some directionality.

A second limitation in this work is the presence of motion artifact. The motion correction algorithm applied in this work was found to significantly reduce the anatomical noise structure in subtracted registered images compared to subtracted unregistered images. However, the algorithm in not perfect, and even the registered images have residual motion artifact, which can be seen to different degrees in Figs. 9(b) and 9(d). Residual motion artifact is almost certainly a contributing factor to the measured anatomical noise in the clinical images, and as such the intrinsic anatomical noise from the tissue and contrast agent uptake has not been measured directly. We feel that it is nonetheless informative to characterize the total anatomical noise, including that from motion, in CEDM clinical images because motion artifact is known to affect lesion detection, and is another "noise" source. However, the amount of motion artifact will vary depending on the imaging protocol, the cooperation of the patient and the motion correction algorithm. For the purposes of system modeling it would be ideal to have anatomical noise values that are true reflections of the intrinsic tissue structure to simulate a best-case scenario. After application of the motion correction algorithm used in this study, we found a significant average decrease in β of 0.13 in the WS of the SE subtracted images. Given these results, for investigators wishing to perform modeling using the anatomical noise values presented here, we note that the presence of motion artifact likely increases the value of β compared to a motion-free measurement. Therefore, detectability experiments based on the CEDM anatomical noise parameters reported here may yield slightly conservative estimates compared to the ideal motion-free situation.

VI. CONCLUSIONS

In this work, we have reported on the anatomical noise in SE CEDM in terms of power law parameters measured on the WS of clinical images. We showed that the process of image subtraction, the presence of an iodinated contrast agent, and the time after contrast agent administration are all important factors that determine the magnitude and structure of the anatomical noise in normal breast tissue in SE CEDM. Image subtraction was demonstrated to lower β from an initial value of 3.1 in the precontrast images to between about 1.1 and 1.8 in the subtracted images, depending on the postcontrast imaging time. While the subtracted images have a greater anatomical noise magnitude, α, than either of the input images, this magnitude is smaller than that of conventional DM by about a factor of 2. We showed that the reduced α in unprocessed HE images compared to DM results from decreased contrast between breast tissues at the higher x-ray spectrum energies.

It was seen that the presence of contrast agent in breast tissues significantly influences the anatomical noise in unprocessed CEDM images, increasing α, and decreasing β at early time points after injection. In the subtracted images, β was found to vary in a quadratic relationship with the time after contrast administration. Consistent power law parameters were observed between two independent pilot studies, which were indistinguishable at equivalent time points. Given that this concordance was obtained despite differing injection protocols, we conclude that small variations on the contrast injection protocol do not significantly affect the anatomical noise.

The power law parameters quantified in this study may be useful as inputs for cascaded systems analysis of SE CEDM and for the generation of synthetic mammographic structures for realistic modeling and optimization of this modality. Given the decrease in β with image subtraction

TABLE IV. Dromain *et al*. study SE CEDM power law analysis results from 20 cases, without a system MTF correction applied. These parameters are imaging system-dependent.

	Unprocessed				SE subtracted			
Time (s)	$\bar{\beta}$	$\sigma(\beta)$	$\bar{\alpha}$ (mm^2)	$\sigma(\alpha)$	$\bar{\beta}$	$\sigma(\beta)$	$\bar{\alpha}$ (mm^2)	$\sigma(\alpha)$
0	3.19	0.41	0.6×10^{-6}	0.3×10^{-6}	N/A		N/A	
30	2.99	0.38	1.0×10^{-6}	0.8×10^{-6}	1.18	0.33	6.7×10^{-6}	6.4×10^{-6}
90	2.98	0.33	1.0×10^{-6}	0.7×10^{-6}	1.48	0.30	5.6×10^{-6}	3.7×10^{-6}
150	3.00	0.29	1.0×10^{-6}	0.5×10^{-6}	1.60	0.36	5.4×10^{-6}	3.3×10^{-6}
240	3.02	0.29	1.0×10^{-6}	0.4×10^{-6}	1.72	0.38	5.5×10^{-6}	3.4×10^{-6}
330	3.05	0.31	1.0×10^{-6}	0.4×10^{-6}	1.74	0.46	6.1×10^{-6}	3.7×10^{-6}
420	3.08	0.30	0.9×10^{-6}	0.4×10^{-6}	1.91	0.52	5.1×10^{-6}	2.8×10^{-6}

TABLE V. Jong *et al*. study SE CEDM power law analysis results from 22 cases, without a system MTF correction applied. These parameters are imaging system-dependent.

	Unprocessed				SE subtracted			
Time (s)	$\bar{\beta}$	$\sigma(\beta)$	$\bar{\alpha}$ (mm^2)	$\sigma(\alpha)$	$\bar{\beta}$	$\sigma(\beta)$	$\bar{\alpha}$ (mm^2)	$\sigma(\alpha)$
0	3.17	0.27	0.7×10^{-6}	0.3×10^{-6}	N/A		N/A	
60	3.05	0.31	1.1×10^{-6}	0.5×10^{-6}	1.44	0.45	5.5×10^{-6}	4.2×10^{-6}
180	3.04	0.30	1.2×10^{-6}	0.6×10^{-6}	1.53	0.43	6.9×10^{-6}	4.1×10^{-6}
300	3.03	0.30	1.3×10^{-6}	0.6×10^{-6}	1.60	0.40	7.8×10^{-6}	4.8×10^{-6}
420	3.04	0.28	1.3×10^{-6}	0.6×10^{-6}	1.69	0.40	7.9×10^{-6}	4.7×10^{-6}
600	3.07	0.32	1.4×10^{-6}	0.7×10^{-6}	1.84	0.38	7.8×10^{-6}	4.5×10^{-6}

demonstrated here, and the established relationship between β and lesion detectability, future work will investigate β as an image quality metric for CEDM to quantify background tissue suppression performance.

ACKNOWLEDGMENTS

The authors gratefully acknowledge Albert Tyson for his work on region of interest identification, Olivier Alonzo-Proulx for his contribution of an algorithm to determine the constant thickness region of the breast, and Giovanni Palma for his preparation of the clinical datasets. Also thanks to Sylvie Saab-Puong and Răzvan Iordache for useful discussions. This project is funded by the Canadian Breast Cancer Foundation – Ontario Region. The work described here has drawn directly from a project supported by The Ontario Institute for Cancer Research (PI, James Mainprize). This work is supported in part through a research collaboration with GE Healthcare.

APPENDIX: SYSTEM-DEPENDENT ANATOMICAL NOISE

To allow for a direct comparison between the power law parameter measurements in this study and those published in the literature without a MTF correction,[4,5] the system-dependent power law parameters (no MTF correction) for each SE CEDM image dataset are summarized in Tables IV and V.

[a]Author to whom correspondence should be addressed. Electronic mail: melissa.hill@sri.utoronto.ca

[1]A. E. Burgess, "Mammographic structure: Data preparation and spatial statistics analysis," Proc. SPIE **3661**, 642–653 (1999).
[2]F. O. Bochud, J. F. Valley, F. R. Verdun, C. Hessler, and P. Schnyder, "Estimation of the noisy component of anatomical backgrounds," Med. Phys. **26**, 1365–1370 (1999).
[3]J. J. Heine, S. R. Deans, R. P. Velthuizen, and L. P. Clarke, "On the statistical nature of mammograms," Med. Phys. **26**, 2254–2265 (1999).
[4]K. G. Metheany, C. K. Abbey, N. Packard, and J. M. Boone, "Characterizing anatomical variability in breast CT images," Med. Phys. **35**, 4685–4694 (2008).
[5]E. Engstrom, I. Reiser, and R. Nishikawa, "Comparison of power spectra for tomosynthesis projections and reconstructed images," Med. Phys. **36**, 1753–1758 (2009).
[6]L. Chen, C. K. Abbey, A. Nosrateih, K. K. Lindfors, and J. M. Boone, "Anatomical complexity in breast parenchyma and its implications for optimal breast imaging strategies," Med. Phys. **39**, 1435–1441 (2012).
[7]I. Reiser, S. Lee, and R. M. Nishikawa, "On the orientation of mammographic structure," Med. Phys. **38**, 5303–5306 (2011).
[8]A. E. Burgess, F. L. Jacobson, and P. F. Judy, "Human observer detection experiments with mammograms and power-law noise," Med. Phys. **28**, 419–437 (2001).
[9]A. E. Burgess and P. F. Judy, "Signal detection in power-law noise: Effect of spectrum exponents," J. Opt. Soc. Am. A **24**, B52–B60 (2007).
[10]L. Chen, C. K. Abbey, and J. M. Boone, "Association between power law coefficients of the anatomical noise power spectrum and lesion detectability in breast imaging modalities," Phys. Med. Biol. **58**, 1663–1681 (2013).
[11]S. Richard, J. H. Siewerdsen, D. A. Jaffray, D. J. Moseley, and B. Bakhtiar, "Generalized DQE analysis of radiographic and dual-energy imaging using flat-panel detectors," Med. Phys. **32**, 1397–1413 (2005).
[12]G. J. Gang, D. J. Tward, J. Lee, and J. H. Siewerdsen, "Anatomical background and generalized detectability in tomosynthesis and cone-beam CT," Med. Phys. **37**, 1948–1965 (2010).
[13]M. Skarpathiotakis, M. J. Yaffe, A. K. Bloomquist, D. Rico, S. Muller, A. Rick, and F. Jeunehomme, "Development of contrast digital mammography," Med. Phys. **29**, 2419–2426 (2002).
[14]J. M. Lewin, P. K. Isaacs, V. Vance, and F. J. Larke, "Dual-energy contrast-enhanced digital subtraction mammography: Feasibility," Radiology **229**, 261–268 (2003).
[15]M. A. Gimbrone, S. B. Leapman, R. S. Cotran, and J. Folkman, "Tumor dormancy in vivo by prevention of neovascularization," J. Exp. Med. **136**, 261–276 (1972).
[16]F. Yuan, M. Dellian, D. Fukumura, M. Leunig, D. A. Berk, V. P. Torchilin, and R. K. Jain, "Vascular permeability in a human tumor xenograft: Molecular size dependence and cutoff size," Cancer Res. **55**, 3752–3756 (1995).
[17]D. Mehta and A. B. Malik, "Signaling mechanisms regulating endothelial permeability," Physiol. Rev. **86**, 279–367 (2006).
[18]R. A. Jong, M. J. Yaffe, M. Skarpathiotakis, R. S. Shumak, N. M. Danjoux, and A. Gunesekara, "Contrast-enhanced digital mammography: Initial clinical experience," Radiology **228**, 842–850 (2003).
[19]C. Dromain, C. Balleyguier, S. Muller, M.-C. Mathieu, F. Rochard, P. Opolon, and R. Sigal, "Evaluation of tumor angiogenesis of breast carcinoma using contrast-enhanced digital mammography," Am. J. Roentgenol. **187**, 528–537 (2006).
[20]F. Diekmann, S. Diekmann, F. Jeunehomme, S. Muller, B. Hamm, and U. Bick, "Digital mammography using iodine-based contrast media: Initial clinical experience with dynamic contrast medium enhancement," Invest. Radiol. **40**, 397–404 (2005).
[21]C. D. Arvanitis and R. Speller, "Quantitative contrast-enhanced mammography for contrast medium kinetics studies," Phys. Med. Biol. **54**, 6041–6064 (2009).
[22]A.-K. Carton, J. Li, M. Albert, S. Chen, and A. D. A. Maidment, "Quantification for contrast-enhanced digital breast tomosynthesis," Proc. SPIE **6142**, 61420D (2006).
[23]S. C. Kappadath and C. C. Shaw, "Dual-energy digital mammography for calcification imaging: Scatter and nonuniformity corrections," Med. Phys. **32**, 3395–3408 (2005).
[24]V. King, J. D. Brooks, J. L. Bernstein, A. S. Reiner, M. C. Pike, and E. A. Morris, "Background parenchymal enhancement at breast MR imaging and breast cancer risk," Radiology **260**, 50–60 (2011).
[25]S. A. Jansen, V. C. Lin, M. L. Giger, H. Li, G. S. Karczmar, and G. M. Newstead, "Normal parenchymal enhancement patterns in women undergoing MR screening of the breast," Eur. Radiol. **21**, 1374–1382 (2011).

[26]N. M. Hambly, L. Liberman, D. D. Dershaw, S. Brennan, and E. A. Morris, "Background parenchymal enhancement on baseline screening breast MRI: Impact on biopsy rate and short-interval follow-up," Am. J. Roentgenol. **196**, 218–224 (2011).
[27]W. B. Demartini, F. Liu, S. Peacock, P. R. Eby, R. L. Gutierrez, and C. D. Lehman, "Background parenchymal enhancement on breast MRI: Impact on diagnostic performance," Am. J. Roentgenol. **198**, W373–W380 (2012).
[28]A.-K. Carton, P. Bakic, C. Ullberg, H. Derand, and A. D. A. Maidment, "Development of a physical 3D anthropomorphic breast phantom," Med. Phys. **38**, 891–896 (2011).
[29]K. Bliznakova, Z. Kolitsi, and N. Pallikarakis, "Dual-energy mammography: Simulation studies," Phys. Med. Biol. **51**, 4497–4515 (2006).
[30]P. R. Bakic, C. Zhang, and A. D. A. Maidment, "Development and characterization of an anthropomorphic breast software phantom based upon region-growing algorithm," Med. Phys. **38**, 3165–3176 (2011).
[31]N. Kiarashi, Y. Lin, W. P. Segars, S. V. Ghate, L. Ikejimba, B. Chen, J. Y. Lo, J. T. Dobbins III, L. W. Nolte, and E. Samei, "Development of a dynamic 4D anthropomorphic breast phantom for contrast-based breast imaging," Proc. SPIE **8313**, 83130C (2012).
[32]E. Fredenberg, M. Hemmendorff, B. Cederström, M. Åslund, and M. Danielsson, "Contrast-enhanced spectral mammography with a photon-counting detector," Med. Phys. **37**, 2017–2029 (2010).
[33]N. Allec, S. Abbaszadeh, and K. S. Karim, "Analysis of multilayer and single layer x-ray detectors for contrast-enhanced mammography using imaging task," Proc. SPIE **7961**, 796111 (2011).
[34]T. E. Yankeelov, M. Lepage, A. Chakravarthy, E. E. Broome, K. J. Niermann, M. C. Kelley, I. Meszoely, I. A. Mayer, C. R. Herman, K. McManus, R. R. Price, and J. C. Gore, "Integration of quantitative DCE-MRI and ADC mapping to monitor treatment response in human breast cancer: Initial results," Magn. Reson. Imaging **25**, 1–13 (2007).
[35]B. Brooksby, B. W. Pogue, S. Jiang, H. Dehghani, S. Srinivasan, C. Kogel, T. D. Tosteson, J. Weaver, S. P. Poplack, and K. D. Paulsen, "Imaging breast adipose and fibroglandular tissue molecular signatures by using hybrid MRI-guided near-infrared spectral tomography," Proc. Natl. Acad. Sci. U.S.A. **103**, 8828–8833 (2006).
[36]J.-P. Delille, P. J. Slanetz, E. D. Yeh, D. B. Kopans, and L. Garrido, "Breast cancer: Regional blood flow and blood volume measured with magnetic susceptibility-based MR imaging–initial results," Radiology **223**, 558–565 (2002).
[37]J. G. Mainprize and M. J. Yaffe, "Cascaded analysis of signal and noise propagation through a heterogeneous breast model," Med. Phys. **37**, 5243–5250 (2010).
[38]W. Krause and G. Schuhmann-Gampieri, "Pharmacokinetics of contrast media," in *Contrast Media in Practice*, edited by P. Dawson and W. Clauss (Springer, Berlin, 1998), pp. 31–39.
[39]P. C. Johns and M. J. Yaffe, "X-ray characterisation of normal and neoplastic breast tissues," Phys. Med. Biol. **32**, 675–695 (1987).
[40]T. E. Yankeelov, W. D. Rooney, W. Huang, J. P. Dyke, X. Li, A. Tudorica, J.-H. Lee, J. A. Koutcher, and C. S. Springer, "Evidence for shutter-speed variation in CR bolus-tracking studies of human pathology," NMR Biomed. **18**, 173–185 (2005).
[41]J. W. Baish and R. K. Jain, "Fractals and Cancer," Cancer Res. **60**, 3683–3688 (2000).
[42]J. J. Going, "Escaping from Flatland: Clinical and biological aspects of human mammary duct anatomy in three dimensions," J. Pathol. **203**, 538–544 (2004).
[43]N. Allec, S. Abbaszadeh, C. C. Scott, J. M. Lewin, and K. S. Karim, "Including the effect of motion artifacts in noise and performance analysis of dual-energy contrast-enhanced mammography," Phys. Med. Biol. **57**, 8405–8425 (2012).
[44]J. Modersitzki, *FAIR: Flexible Algorithms for Image Registration* (SIAM, Philadelphia, PA, 2009), p. 210.
[45]J. G. Mainprize, A. H. Tyson, and M. J. Yaffe, "The relationship between anatomic noise and volumetric breast density for digital mammography," Med. Phys. **39**, 4660–4668 (2012).
[46]O. Alonzo-Proulx, J. G. Mainprize, N. J. Packard, J. M. Boone, A. Al-Mayah, K. Brock, and M. J. Yaffe, "Development of a peripheral thickness estimation method for volumetric breast density measurements in mammography using a 3D finite element breast model," Lect. Notes Comput. Sci. **6136**, 467–473 (2010).
[47]H. M. Jensen, "On the origin and progression of human breast cancer," Am. J. Obstet. Gynecol. **154**, 1280–1284 (1986).
[48]G. Wu, J. G. Mainprize, and M. J. Yaffe, "Spectral analysis of mammographic images using a multitaper method," Med. Phys. **39**, 801–810 (2012).
[49]J. T. Dobbins, D. L. Ergun, L. Rutz, D. A. Hinshaw, H. Blume, and D. C. Clark, "DQE(f) of four generations of computed radiography acquisition devices," Med. Phys. **22**, 1581–1593 (1995).
[50]D. B. Percival and A. T. Walden, *Spectral Analysis for Physical Applications: Multitaper and Conventional Univariate Techniques* (Cambridge University Press, Cambridge, England, 1993), p. 208.
[51]P. R. Bevington and D. K. Robinson, *Data Reduction and Error Analysis for the Physical Sciences*, 3rd ed. (McGraw-Hill, New York, 2003), p. 138.
[52]Y.-H. Hu and W. Zhao, "A 3D linear system model for the optimization of dual-energy contrast-enhanced digital breast tomosynthesis," Proc. SPIE **7961**, 79611C (2011).
[53]S. Vedantham, L. Shi, S. J. Glick, and A. Karellas, "Scaling-law for the energy dependence of anatomic power spectrum in dedicated breast CT," Med. Phys. **40**, 011901 (8pp.) (2013).
[54]O. Alonzo-Proulx, N. Packard, J. M. Boone, A. Al-Mayah, K. K. Brock, S. Z. Shen, and M. J. Yaffe, "Validation of a method for measuring the volumetric breast density from digital mammograms," Phys. Med. Biol. **55**, 3027–3044 (2010).
[55]J. A. Rowlands, W. G. Ji, and W. Zhao, "Effect of depth dependent modulation transfer function and K- fluorescence reabsorption on the detective quantum efficiency of indirect conversion flat panel x-ray imaging systems using CsI," Proc. SPIE **4320**, 257–267 (2001).
[56]J. M. Boone, K. K. Lindfors, V. N. Cooper, and J. A. Seibert, "Scatter/primary in mammography: Comprehensive results," Med. Phys. **27**, 2408–2416 (2000).
[57]E. Samei, M. J. Flynn, and D. A. Reimann, "A method for measuring the presampled MTF of digital radiographic systems using an edge test device," Med. Phys. **25**, 102–113 (1998).
[58]N. W. Marshall, P. Monnin, H. Bosmans, F. O. Bochud, and F. R. Verdun, "Image quality assessment in digital mammography. Part I. Technical characterization of the systems," Phys. Med. Biol. **56**, 4201–4220 (2011).
[59]G. J. Gang, W. Zbijewski, J. Webster Stayman, and J. H. Siewerdsen, "Cascaded systems analysis of noise and detectability in dual-energy cone-beam CT," Med. Phys. **39**, 5145–5156 (2012).
[60]J. M. Boone, T. R. Fewell, and R. J. Jennings, "Molybdenum, rhodium, and tungsten anode spectral models using interpolating polynomials with application to mammography," Med. Phys. **24**, 1863–1874 (1997).
[61]S. C. Chen, A.-K. Carton, M. Albert, E. F. Conant, M. D. Schnall, and A. D. A. Maidment, "Initial clinical experience with contrast-enhanced digital breast tomosynthesis," Acad. Radiology **14**, 229–238 (2007).
[62]C.-W. Ryu, J. K. Kim, S. J. Kim, J. H. Lee, J. H. Kim, H. Il Ha, and D. C. Suh, "Head and neck vascular lesions: Characterization of the flow pattern by the use of three-phase CT," Korean J. Radiol. **10**, 323–332 (2009).
[63]J. A. Brink, "Contrast optimization and scan timing for single and multidetector-row computed tomography," J. Comput. Assist.Tomogr. **27**, S3–S8 (2003).
[64]N. Allec, S. Abbaszadeh, J. M. Lewin, and K. S. Karim, "Motion artifacts in dual-energy contrast-enhanced mammography," Proc. SPIE **8313**, 83134P (2012).
[65]M. L. Hill, J. G. Mainprize, and M. J. Yaffe, "An observer model for lesion detectability in contrast-enhanced digital mammography," Lect. Notes Comput. Sci. **6136**, 720–727 (2010).